

1 **A fully Lagrangian formulation for fluid-structure**
2 **interaction problems with free-surface flows and**
3 **fracturing solids**

4 **Alejandro Cornejo · Alessandro Franci ·**
5 **Francisco Zárate · Eugenio Oñate**

6
7 Received: date / Accepted: date

8 **Abstract** This paper presents a novel coupled formulation for fluid-structure
9 interaction (FSI) problems involving free-surface fluid flows, fracture phenom-
10 ena, solid mutual contact and large displacements. The numerical formulation
11 combines three different Lagrangian computational methods. The Particle Fi-
12 nite Element Method (PFEM) is used to solve the free-surface fluid flow,
13 a Finite Element Method (FEM) with smoothed isotropic damage model is
14 employed for the solution of solid structures and debris, finally, the Discrete
15 Element Method (DEM) is used to manage the contact interaction between
16 different solid boundaries, including the new ones generated by propagating
17 cracks. The proposed method has a high potential for the prediction of the
18 structural damages on civil constructions caused by natural hazards, such as
19 floods, tsunami waves or landslides. Its application field can also be extended
20 to fracture phenomena in structures and soils/rocks arising from explosions
21 or hydraulic fracking processes. Several numerical examples are presented to
22 show the validity and accuracy of the numerical technique proposed.

23 **Keywords** Fracture Mechanics · Free-Surface Flow · Fluid-Structure
24 Interaction · Discrete Element Method · Particle Finite Element Method

25 **1 Introduction**

26 This work presents a new coupled numerical method for the simulation of
27 structures collapsing and fracturing under the impact of free-surface fluids.
28 This type of FSI problems is of high interest for different engineering applica-

Alejandro Cornejo Velázquez
International Centre for Numerical Methods in Engineering
Carrer del Gran Capità, S/N, 08034 Barcelona
Tel.: +34 934 01 74 95
E-mail: acornejo@cimne.upc.edu

tions and, in particular, for the prediction of the damages on civil infrastructures affected by natural hazards, like floods, tsunami waves, or landslides.

The numerical simulation of these multi-coupled problems is challenging due to their high non-linearity and the complexity of the involved phenomena. Indeed, the numerical method must be able to deal with free-surface flows undergoing large changes of topology and interacting with structures that can break and disintegrate into smaller solid debris which, in turn, may eventually hit other structures.

The complexity of this scenario explains the reduced number of computational methods for FSI problems with fracture phenomena available in the literature. Most of these works are focused on the structural failure of pipes and vessels subjected to shocks and explosions [53, 51, 50, 52, 48, 49, 54]. Another important research area in this field refers to the simulation of hydraulic fracture processes, see [57, 58, 60, 59, 75, 76]. On the other hand, a smaller number of works analyzed the collapse of civil structures caused by the impact of free-surface fluid flows, which is the main focus of the present work. In [56], a FSI formulation with a phase-field fracture model was proposed for the structural failure caused by the impact of fluid flows in closed domains. In [55], similar problems were analyzed considering also the fragmentation of the structure due to the cracks propagation. In [63], free-surface flows were also considered using a coupled Smoothed Particle Hydrodynamics - Discrete Element Method (SPH-DEM) model. Other SPH-based works analyzed the effect of tsunami waves on civil infrastructures, especially bridges, although fracture phenomena were not taken into account [45, 44, 43]. Still in this research line, it is worth to mention the following coupled methods based on SPH [62], Immersed Particle Method (IBM) [64, 65] and DEM-LBM (Lattice Boltzman Method) [66].

The Particle Finite Element Method (PFEM) [39] has also been used to model similar fluid-solid interaction, such as in [19, 7], but without modeling fracture phenomena. On the other hand, in the coupled PFEM-DEM model proposed in [46, 47] for bed erosion processes in river dynamics, the river bed domain was allowed to suffer changes of topology due to the erosion induced by the fluid flow. However, the detached parts could be modeled either as a set of dimensionless DEM particles or as rigid bodies, and not as deformable solids capable of fracturing again, as it is done in the present work.

The FSI problem is here solved with a novel hybrid strategy that combines three different Lagrangian numerical methods. The free-surface flow problem is solved with the stabilized PFEM formulation presented in [7], while the solid deformation, fracture and frictional contact effect are modeled by combining a Finite Element Method (FEM) with smoothed isotropic damage model [3, 16] and a Discrete Element Method (DEM) [13–15], in the spirit of the so-called FEM-DEM procedure [1–3].

The solution accuracy of FSI problems strictly depends on the capability of the numerical method to track the evolving fluid-solid interface and to transfer accurately the boundary conditions. This task is particularly critical for the problems analyzed here because, on the one hand, the fluids have a

75 free surface which changes continuously during the analysis and, on the other
76 hand, the solids can undergo large displacements/rotations and their contours
77 can change significantly due to the propagating cracks and the resulting frag-
78 mentation of the structure. In this work, the fluid-solid interface is detected
79 automatically during the remeshing step of the PFEM solution algorithm. Re-
80 markably, the remeshing procedure used in the PFEM not only improves the
81 quality of the finite element discretization and defines the updated fluid free
82 surface, but also allows to detect the new contact surfaces with the solid bod-
83 ies. The Lagrangian nature of the PFEM guarantees also that all the nodes
84 of the interface belong to both the fluid and the solid meshes. This allows
85 us to avoid projecting nodal variables between the solid and the fluid do-
86 mains. In this sense, the coupled approach here proposed can be classified as
87 a body-fitted conforming-mesh FSI method [27]. Compared to mesh-free [29],
88 non-conforming mesh [28,30] and embedded [38] FSI approaches, body-fitted
89 conforming-mesh algorithms allow for an easier transmission of boundary con-
90 ditions between fluid and solid domains. Nevertheless, these methods generally
91 require a similar size of fluid and solid elements at the interface zone and may
92 lead to mesh distortion issues when applied to large deformation problems. For
93 large and arbitrary motions of the interface, this latter task can become critical
94 for conforming-mesh methods based on Arbitrary Lagrangian-Eulerian (ALE)
95 techniques [36], [71]. Conversely, the PFEM can naturally track the evolving
96 interface and, at the same time, maintains a good discretization, also in the
97 presence of large and unpredictable motion of the fluid-solid interface. This
98 feature represents one of the main advantages of the PFEM for coupled fluid-
99 solid mechanics analysis and also explains the extended use of the method for
100 FSI problems [34,20,31,6,32,33,5].

101 Once the contact interfaces between fluids and solids have been detected,
102 the FSI time step solution is performed through a block Gauss-Seidel (BGS)
103 procedure with Aitken relaxation [61]. The good convergence properties of
104 Aitken schemes have been shown for different types of FSI problems, such as
105 in [73,35,72,74,5]. In this work, a partitioned method has been preferred to a
106 monolithic one to avoid the ill-conditioning of the linear system which could
107 arise due to different orders of magnitude of the physical parameters of the
108 materials. This situation is prone to occur in the problems of interest of this
109 work which involve civil structures that are generally characterized by a high
110 stiffness.

111 The solid mechanics solution is obtained with a FEM-DEM approach that
112 can be classified as a hybrid continuum-discrete formulation for fracture me-
113 chanics. In particular, the onset of cracking is detected using a continuum
114 FEM formulation, while the DEM is used to compute the repulsion forces due
115 to the contact interaction between different solid contours, including those
116 of propagating cracks. Since this work is focused on concrete structures, an
117 isotropic damage model [16] has been used. It is important to remark that dif-
118 ferent damage models could be used with the proposed methodology. Before
119 fracturing, the stiffness degradation of the material and the crack initialization
120 are modeled in a smeared way. During this phase, the mesh topology is not

121 changed and the fracture is represented by stress softening and localization.
 122 When the inelastic energy dissipation reaches the fracture energy in some zones
 123 of the solid, the finite elements contained therein are removed from the mesh
 124 and replaced by a mass-equivalent set of particles, or discrete elements. A sub-
 125 stepping procedure is employed in the time marching scheme to synchronize
 126 the FEM implicit solution and the DEM explicit one.

127 One of the main advantages of the FEM-DEM methodology lays in its ca-
 128 pability to model in a natural way the onset, evolution, merging and branching
 129 of fractures, as well as the eventual detachment of solid blocks, their mutual
 130 contact, and their independent motion under the effect of the fluid flow. This
 131 feature is particularly important for the problems of interest for this work,
 132 because loose solid debris may be at the origin of other damages on structures
 133 or living beings.

134 The paper has been structured as follows. In Section 2, the governing equa-
 135 tions for the solid and the fracture model are presented. In Section 3, the fluid
 136 governing equations and the PFEM scheme are presented. In Section 4, the
 137 FSI solution algorithm through the proposed PFEM-FEM-DEM approach is
 138 described. In Section 5, several numerical examples are analyzed to validate the
 139 overall methodology and to show its potential to real-world problems. Finally,
 140 the concluding remarks of the work are presented in Section 6.

141 2 Solid mechanics problem

142 The solid parts of the domain are solved with a coupled FEM-DEM approach
 143 [1–3]. This method combines a continuum FEM formulation with the DEM
 144 to simulate fracturing solids and the consequent formation of solid debris. In
 145 this section, we first present the governing equations and the FEM solution
 146 scheme, then we describe the damage and fracture models, and finally the
 147 FEM-DEM algorithm to deal with crack propagation and frictional contact
 148 between the interacting solids.

149 2.1 Governing equations for the solid

The solid motion is governed by the linear momentum equations formulated
 in a Total Lagrangian (TL) framework as

$$\rho_s \ddot{\mathbf{u}} - \text{Div} \mathbf{P} - \mathbf{b}_0 = \mathbf{0} \text{ in } \Omega_{s0} \times [0, T] \quad (1)$$

150 where ρ_s is the solid density, \mathbf{u} is the displacement field, \mathbf{P} is the first Piola-
 151 Kirchhoff stress tensor, \mathbf{b}_0 is the external body force per current unit volume
 152 over the undeformed solid configuration Ω_{s0} , and T is the total time duration.

153 A set of initial conditions specifying displacements and velocities at time
 154 $t = 0$ are defined as:

$$\mathbf{u}(t = 0) = \hat{\mathbf{u}}_0 \text{ in } \Omega_0 \quad (2)$$

$$\mathbf{v}(t=0) = \hat{\mathbf{v}}_0 \text{ in } \Omega_0 \quad (3)$$

155 where \mathbf{v} are the velocities, and $\hat{\mathbf{u}}_0$ and $\hat{\mathbf{v}}_0$ are the initial displacements and
156 velocities, respectively.

157 The governing equations set is closed by the following boundary conditions

$$\mathbf{P} \cdot \mathbf{N} = \hat{\mathbf{t}}_0 \text{ in } \Gamma_\sigma \times [0, T] \quad (4)$$

$$\mathbf{u} = \hat{\mathbf{u}} \text{ in } \Gamma_u \times [0, T] \quad (5)$$

158 where \mathbf{N} is the unit normal vector, $\hat{\mathbf{t}}_0$ are the tractions applied on the Neumann
159 boundary Γ_σ , and $\hat{\mathbf{u}}$ are the prescribed displacements to the Dirichlet contours
160 Γ_u .

In this coupled approach, the traction vector $\hat{\mathbf{t}}_0$ is computed as the sum of three different contributions as

$$\hat{\mathbf{t}}_0 = \mathbf{t}_{\text{loads}} + \mathbf{t}_{\text{contact}} + \mathbf{t}_{\text{fluid}} \quad (6)$$

161 where $\mathbf{t}_{\text{loads}}$ are the tractions arising from standard external loads, $\mathbf{t}_{\text{contact}}$
162 are the tractions due to the contact with other solid bodies, and $\mathbf{t}_{\text{fluid}}$ are the
163 tractions induced by the fluid pressures.

164 2.1.1 Finite element solution

165 The solid governing equations (Eq. (1)) are solved with an implicit scheme,
166 using 3-nodded triangular elements in 2D and 4-nodded tetrahedral in 3D.
167 Each time step is solved iteratively for the increments of nodal displacements
168 $\Delta \bar{\mathbf{u}}$ (the upper bar $\bar{\cdot}$ denotes a nodal variable). The derivation of the fully
169 discretized and linearized form of the governing equations is considered out of
170 the scope of the present work. Interested readers may refer to [1–3] for details.
171 For a generic time step $[{}^n t, {}^{n+1} t]$ of duration Δt , the following linear system
172 is solved for each iteration k :

$$\mathbf{K}(\bar{\mathbf{u}}_k) \cdot \Delta \bar{\mathbf{u}}_{k+1} = -\mathbf{r}(\bar{\mathbf{u}}_k). \quad (7)$$

173 being:

$$\mathbf{r}(\bar{\mathbf{u}}_k) = \mathbf{M} \bar{\mathbf{a}}_k + \mathbf{C} \bar{\mathbf{v}}_k + \mathbf{f}_{\text{int}}(\bar{\mathbf{u}}_k) - {}^{n+1} \mathbf{f}_{\text{ext}} - {}^{n+1} \mathbf{f}_{\text{fluid}} - {}^{n+1} \mathbf{f}_{\text{contact}} \quad (8)$$

174 and

$$\mathbf{K}(\bar{\mathbf{u}}_k) = \left[\frac{1}{\beta \Delta t^2} \mathbf{M} + \frac{\gamma}{\beta \Delta t} \mathbf{C} + \mathbf{K}_T(\bar{\mathbf{u}}_k) \right]. \quad (9)$$

175 where $\bar{\mathbf{a}}_k$ are the nodal accelerations computed at the k^{th} iteration, \mathbf{f}_{int} and
176 \mathbf{f}_{ext} are the internal and external forces vectors, respectively, $\mathbf{f}_{\text{fluid}}$ are the
177 equivalent nodal forces due to the fluid pressure, $\mathbf{f}_{\text{contact}}$ are the equivalent
178 contact nodal forces, \mathbf{M} , \mathbf{C} and \mathbf{K}_T are the mass, damping and tangential
179 stiffness matrices, respectively, and the parameters $\beta = 0.25$, $\gamma = 0.5$ have
180 been used.

181 For the sake of completeness, all the variables and matrices introduced in
182 Eqs.(8-9) are defined in Appendix A.

2.2 Damage and fracture models for concrete

For the fracture analysis of concrete, the isotropic damage model proposed by Oliver et al. [16] for crack propagation has been used. We would like to remark that other damage models could be included in the proposed methodology to represent different material behaviors. Nevertheless, this is considered out of the scope of the present work and it is left for future developments.

In this model, the internal damage variable d^{elem} describes the material degradation, varying from 0 (intact material) to 1 (fully damaged material). The constitutive model relates the Green-Lagrange strain tensor \mathbf{E} with the second Piola-Kirchhoff stress tensor \mathbf{S} as:

$$\mathbf{S} = \mathbf{C}_s \mathbf{E} = (1 - d^{elem}) \mathbf{C}_0 \mathbf{E} = (1 - d^{elem}) \hat{\mathbf{S}}, \quad (10)$$

where $\hat{\mathbf{S}}$ is the effective second Piola-Kirchhoff stress tensor, $\mathbf{C}_s = (1 - d) \mathbf{C}_0$ is the secant constitutive tensor, and \mathbf{C}_0 the elastic constitutive tensor.

The damage parameter d is computed by evaluating the effective stresses at the mid-sides of the adjacent elements. This allows us to obtain super-convergence values of the stresses at these points [25, 26]. This means that the error of the computed values at these points decreases with a higher rate of convergence.

Fig. 1 shows the scheme to compute the effective stress tensor $\hat{\mathbf{S}}$ at the edges from the stress tensors evaluated at the integration points of the finite elements sharing that edge as:

$$\hat{\mathbf{S}}^{edge} = \frac{1}{n_{elem}} \sum_{i=1}^{n_{elem}} \hat{\mathbf{S}}^{neig,i} \quad (11)$$

where n_{elem} is the number of elements sharing the edge.

The effective stress tensor at each element edge is also used to evaluate whether the material is in elastic or inelastic regime basing on the following general definition of yield surface Φ

$$\Phi = f(\hat{\mathbf{S}}^{edge}) - \sigma^{\tau,edge} \leq 0 \quad (12)$$

where $f(\hat{\mathbf{S}}_{edge})$ is the so-called equivalent effective stress whose definition depends on the yield surface of interest and $\sigma^{\tau,edge}$ is the stress threshold which is computed as:

$$\sigma^{\tau,edge} = \max(\sigma^{\tau_0}, \max(f(\hat{\mathbf{S}}^{edge})_t)) \quad t \in [0, T], \quad (13)$$

where σ^{τ_0} is the initial yield strength of the material.

This definition guarantees that the material threshold is the maximum historical equivalent stress achieved and also ensures the irreversibility of the damaging process.

The internal damage variable d is also evaluated at each edge of the elements using the following exponential softening law:

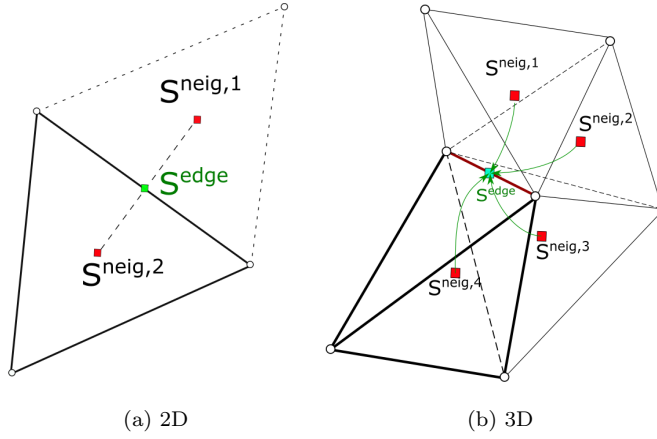


Fig. 1: *Super-convergent* points. Graphical representation of the effective stress smoothing at the FE edge. The subscript "neig" stands for neighbor element.

$$d^{edge}(\hat{\mathbf{S}}^{edge}) = 1 - \frac{\sigma^{\tau_0}}{f(\hat{\mathbf{S}}^{edge})} \exp\left(A \left(1 - \frac{f(\hat{\mathbf{S}}^{edge})}{\sigma^{\tau_0}}\right)\right) \quad (14)$$

216 in which the parameter A is determined from the energy dissipated in a
217 uni-axial tension test as [16]

$$A = \left(\frac{G_f E}{\hat{l}(\sigma^{\tau_0})^2} - \frac{1}{2}\right)^{-1} \quad (15)$$

218 in which G_f is the specific fracture energy per unit area (taken as a material
219 property), E is the Young modulus, \hat{l} is the characteristic length of the element,
220 and σ^{τ_0} is the initial tensile yield strength.

221 The elemental damage is computed after evaluating the damage variables at
222 all its edges and for all the possible fracture modes. Fig. 2 shows a qualitative
223 representation of the possible failure modes that can occur in 2D and 3D
224 geometries. The figure shows that, in 2D, only 2-edged modes are allowed,
225 whereas both 3-edged and 4-edged modes can occur in 3D. In 2D, the elemental
226 damage will be always the mean value of the two highest damage variables of
227 the three edges of the element, thus:

$$d^{elem} = \frac{1}{2} \left(d_{max}^{edge} + d_{max-1}^{edge}\right) \quad (16)$$

228 where d_{max}^{edge} and d_{max-1}^{edge} are the two highest damage variables of the three
229 edges of the triangular finite element.

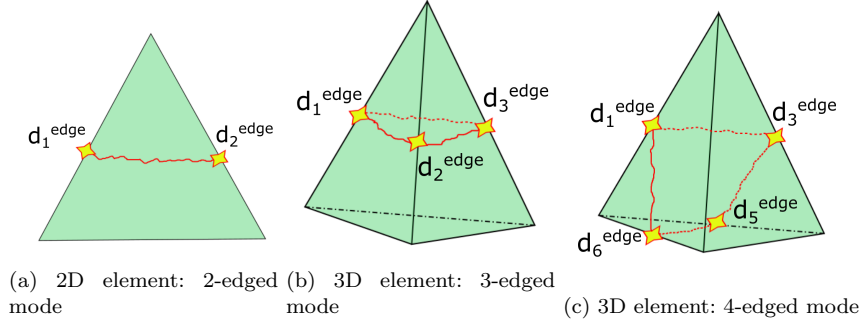


Fig. 2: Different fracture modes in 2D and 3D element geometries [3].

Analogously, in three dimensional meshes, the elemental damage d^{elem} is computed as the maximum of the following seven fracture modes d_i^{elem} :

$$d_1^{elem} = \frac{1}{3}(d_1^{edge} + d_2^{edge} + d_3^{edge}) \quad (17a)$$

$$d_2^{elem} = \frac{1}{3}(d_1^{edge} + d_4^{edge} + d_5^{edge}) \quad (17b)$$

$$d_3^{elem} = \frac{1}{3}(d_2^{edge} + d_4^{edge} + d_6^{edge}) \quad (17c)$$

$$d_4^{elem} = \frac{1}{3}(d_3^{edge} + d_5^{edge} + d_6^{edge}) \quad (17d)$$

$$d_5^{elem} = \frac{1}{4}(d_2^{edge} + d_3^{edge} + d_4^{edge} + d_5^{edge}) \quad (17e)$$

$$d_6^{elem} = \frac{1}{4}(d_1^{edge} + d_2^{edge} + d_5^{edge} + d_6^{edge}) \quad (17f)$$

$$d_7^{elem} = \frac{1}{4}(d_1^{edge} + d_3^{edge} + d_4^{edge} + d_6^{edge}). \quad (17g)$$

230

231 If the resulting elemental damage becomes higher than a pre-fixed thresh-
 232 old (blue $d^{elem} > 0.98$), this element is removed from the FE mesh. A high
 233 value of the damage threshold has been chosen with the aim of minimizing
 234 the perturbation of the equilibrium state reached at the previous time step
 235 computation. Once an element is removed from the mesh, a set of DE parti-
 236 cles (three in 2D and four in 3D) is automatically placed over the nodes of
 237 the erased FE [1–3]. As it will be described more in detail in the next section,
 238 these particles are used to compute the contact forces between different solids,
 239 or between different parts of the same structure.

240

241 It is important to note that, since the crack path is determined by the suc-
 242 cessive element erosion, the crack width is directly dependent on the element
 243 size. This limitation has been circumvented in Cornejo et al. [3] by adding an
 244 adaptive remeshing technique to this algorithm. However, due to the need of
 245 maintaining a similar mesh size for the fluid and the solid elements placed at
 246 the interface for the whole analysis (see Section 3.3), this procedure has not
 been employed in this FSI approach.

2.3 Contact forces computation with the DEM

In order to prevent the mutual penetration of solid elements faces, a set of discrete elements is overlapped to the boundary nodes of the solid. In the case of a propagating fracture, additional discrete elements are placed over the new boundary nodes of the crack. Once a DE detects an active contact with another solid boundary, either with another DE or a FE edge, a repulsive force is computed and transmitted to the FEM nodes.

The DEM procedure used within the FEM-DEM formulation is based on the works of Casas et al [17], Oñate et al [13] and Thornton et al. [18].

Considering two colliding particles, whose coordinates are \mathbf{r}_1 and \mathbf{r}_2 , the normal vector that aligns the centres of the spheres is computed as follows:

$$\mathbf{n}_{21} = \frac{\mathbf{r}_2 - \mathbf{r}_1}{\|\mathbf{r}_2 - \mathbf{r}_1\|}, \quad \mathbf{n}_{21} = -\mathbf{n}_{12}. \quad (18)$$

The normal indentation δ_n between the discrete particles is computed as:

$$\delta_n = R_1 + R_2 - \|\mathbf{r}_{21}\|, \quad \mathbf{r}_{21} = \mathbf{r}_2 - \mathbf{r}_1. \quad (19)$$

where R_i is the radius of particle i .

The total contact force between two particles $\mathbf{F}_{contact}$ is decomposed into its normal and tangential components as:

$$\mathbf{F}_{contact} = F_n \mathbf{n} + F_t \mathbf{t} \quad (20)$$

The normal component of the contact force F_n is obtained as a combination of an elastic ($F_{n,el}$) and a viscous ($F_{n,damp}$) contribution, *i.e.*:

$$F_n = F_{n,el} + F_{n,damp} \quad (21)$$

Considering a standard Hertzian model, the elastic part is computed as:

$$F_{n,el} = \frac{4}{3} \tilde{R}^{\frac{1}{2}} \tilde{E} \delta_n^{\frac{3}{2}} \quad (22)$$

where $\tilde{R} := (1/R_1 + 1/R_2)^{-1}$, $\tilde{E} = \left(1/\tilde{E}_1 + 1/\tilde{E}_2\right)^{-1}$ with $\tilde{E}_i := E_i/(1 - \nu_i^2)$, being ν_i the Poisson ratio, E the Young modulus and R the radius of each particle.

The viscous damping contribution is computed as:

$$F_{n,damp} = c_n \delta_n^{1/4} \dot{\delta}_n. \quad (23)$$

For particle-particle contact the constant c_n is given by

$$c_n = \gamma \sqrt{8 \tilde{E} \tilde{M} \sqrt{\tilde{R}}} \quad (24)$$

being $\tilde{M} := (1/m_1 + 1/m_2)^{-1}$ and γ a viscous damping coefficient.

On the other hand, the tangential component of the contact force (Eq. 20) is computed as:

$$\mathbf{F}_t = F_{t,el} \mathbf{t}_d + F_{t,damp} \mathbf{t}_\nu \quad (25)$$

where the directions \mathbf{t}_d and \mathbf{t}_ν are based on the kinematics during tangential deformation [13].

The elastic tangential contribution is obtained by:

$$F_{t,el} = \delta_n^{1/2} \int 8G \dot{\delta} dt \quad (26)$$

being G the shear modulus. The tangential viscous contribution as

$$F_{t,damp} = c_t \delta_n^{1/4} \dot{\delta}_t \quad (27)$$

with

$$c_t = 2\gamma \sqrt{8\tilde{G}\tilde{M}\sqrt{\tilde{R}}} \quad (28)$$

where $\tilde{G} = G/(4 - 2\nu)$ and $G = E/(2 + 2\nu)$.

2.4 FEM-DEM solution scheme

As the FEM solution is obtained via an implicit scheme and the DEM with an explicit one, the time step increment used in the two methods may be of different orders of magnitude. Thus, to optimize the computational performance of the method, a sub-stepping procedure is used. Thus, for each time step increment of the FEM solution (Δt), the DEM problem is solved several times using a smaller time increment (Δt_e). Note that the time step used for the FEM solid solution is the same as the one used for the implicit PFEM solution of the fluid parts of the domain.

The iterative FEM solution (Eqs.(7)-(9)) is obtained considering the contact forces computed at the end of the previous time step. We remark that the contact forces could be also computed implicitly. However, this would lead to a further increase in the computational cost of the analysis, due to the required iterations of the FEM-DEM solution scheme. Furthermore, it should be considered that the time increments used in the FSI analyses of this work are typically small, especially during the structural failure and post-failure scenarios, and this limits the effect of our simplification.

Once the numerical solution of the solid has converged, the kinematic information of the FEM boundary nodes is transferred to the respective discrete element. In case of having an active solid-solid interaction, the kinematic information is used to compute the new contact forces through a sub-stepping loop. At each explicit time step (${}^e t$), the kinematic information of each particle is updated by interpolating the FEM results obtained at the previous time step (${}^n t$) and those of the converged one (${}^{n+1} t$). This information is used to compute the corresponding contact force contribution $\mathbf{F}_{contact}$ from Eq.(20), which is added to the accumulated impulse $\mathbf{I}({}^e t)$ as

$$\mathbf{I}({}^e t) = \mathbf{I}({}^{e-1} t) + \Delta t_e \cdot \mathbf{F}_{contact} \quad (29)$$

Once the sub-stepping is finalized (${}^e t = {}^{n+1}t$), the contact forces needed in the FEM solution of the following time step (Eq.8) are computed as

$$\mathbf{f}_{contact} = \frac{\mathbf{I}({}^e t)}{\Delta t} \quad (30)$$

282

Algorithm 1 summarizes the solution scheme of the FEM-DEM method.

Algorithm 1: FEM-DEM solution algorithm for a generic time step $[{}^n t; {}^{n+1}t]$ of duration Δt .

```

Initialization of the implicit transient dynamic scheme for the FEM:
 $k \leftarrow 0$ ,  $\bar{\mathbf{u}}_0 \leftarrow {}^n \bar{\mathbf{u}}$ 
Apply the DE contact forces obtained at the last time step as equivalent nodal
force for the FEM ( ${}^n \mathbf{f}_{contact}$  of Eq.8)
while  $\|\mathbf{r}_{eff,dyn}\| > tol$  do
  for Elements do
    Compute the effective stresses  $\bar{\boldsymbol{\sigma}} = \mathbf{C}_0 : \boldsymbol{\varepsilon}$ 
    Smoothing of the effective stress field at the FE edges
    Compute the damage  $d$  at the edges by Eq. (14)
    Obtain the elemental damage by Eq. (16)
    Calculate the elemental tangent stiffness matrix  $\mathbf{K}_T^{(e)}$  and internal forces
    vector  $\mathbf{f}_{int}^{(e)}$ 
    Assemble elemental contributions:  $\mathbf{K}_T \leftarrow \mathbf{K}_T^{(e)}$  and  $\mathbf{f}_{int} \leftarrow \mathbf{f}_{int}^{(e)}$ 
  end
  Calculate the displacement increments  $\Delta \mathbf{u}_{k+1} = \mathbf{K}_T^{-1} \mathbf{r}_k$ 
   $k += 1$ 
end
for Elements do
  if Damage  $\geq 0.98$  then
    Erase the FE
    Generate the Discrete Elements (DE) at the nodes of the damaged FE
  end
end
Initialization of the explicit transient dynamic scheme for the DEM
 ${}^e t \leftarrow {}^n t$ 
while  ${}^e t \leq {}^{n+1}t$  do
   ${}^e t += \Delta t_e$ 
  Obtain the FEM kinematic information for the DE by interpolating the FEM
  results between the initial time ( ${}^n t$ ) and the final one ( ${}^{n+1}t$ )
  Compute the contact forces  $\mathbf{F}_{contact}$  using Eq. (20)
  Update the explicit contact impulses at each particle using Eq. (29)
  Integrate the equations of motion for the free particles
  Compute the displacements, velocities, and accelerations of free particles
end
Compute the updated equivalent contact nodal forces  ${}^{n+1} \mathbf{f}_{contact}$  using Eq. (30)

```

283 3 Fluid dynamics problem

284 3.1 Governing equations of the fluid

The governing equations for the fluid dynamics problem are the linear momentum balance and the mass conservation equations. The problem is solved in an Updated Lagrangian framework as in the standard PFEM [19]. Calling Ω_f the updated fluid domain, the fluid governing equations read

$$\rho_f \frac{\partial \mathbf{v}}{\partial t} - \nabla \cdot \boldsymbol{\sigma} - \rho_f \mathbf{g} = \mathbf{0} \quad \text{in } \Omega_f \times (0, T) \quad (31)$$

$$\nabla \cdot \mathbf{v} - \frac{1}{\kappa_f} \frac{\partial p}{\partial t} = 0 \quad \text{in } \Omega_f \times (0, T) \quad (32)$$

285 where \mathbf{v} is the velocity vector, t is the time, $\boldsymbol{\sigma}$ is the fluid Cauchy stress tensor,
 286 \mathbf{g} is the gravity acceleration vector, and ρ_f and κ_f are the fluid density and
 287 bulk modulus, respectively.

For Newtonian fluids, the Cauchy stress tensor is split as

$$\boldsymbol{\sigma} = p\mathbf{I} + 2\mu_f \mathbf{d}' \quad (33)$$

where p is the pressure, \mathbf{I} is the 2^{nd} order identity tensor, μ_f is the fluid dynamic viscosity, and \mathbf{d}' is the deviatoric part of the deformation rate tensor \mathbf{d} computed as

$$\mathbf{d}' = \frac{1}{2} (\nabla \mathbf{v} + (\nabla \mathbf{v})^T) - \frac{1}{3} d_v \mathbf{I} \quad (34)$$

288 where $d_v = \nabla \cdot \mathbf{v}$ is the volumetric deformation rate.

289 Following [20,21,10], the mass conservation equation (Eq.(32)) is here
 290 solved not in the standard divergence-free form of the Navier-Stokes prob-
 291 lem ($\nabla \cdot \mathbf{v} = 0$), but considering a certain (small) compressibility of fluid
 292 material. For values of bulk modulus going to infinity the divergence-free form
 293 of the continuity equation is recovered.

The fluid governing equations are completed by the following boundary conditions at the Dirichlet (Γ_f^v) and Neumann (Γ_f^t) boundaries

$$\begin{aligned} \mathbf{v} &= \hat{\mathbf{v}} && \text{on } \Gamma_f^v \\ \boldsymbol{\sigma} \cdot \mathbf{n} &= \hat{\mathbf{t}} && \text{on } \Gamma_f^t \end{aligned} \quad (35)$$

294 being \mathbf{n} the normal vector to the fluid boundaries, $\hat{\mathbf{v}}$ the prescribed velocities
 295 at the Dirichlet boundaries and $\hat{\mathbf{t}}$ the prescribed tractions at the Neumann
 296 ones.

297 3.2 Finite element solution

298 The fluid governing equations are solved in a standard FEM fashion following
 299 the implicit stabilized velocity-pressure strategy presented in [9]. The domain
 300 is discretized with simplicial elements (triangles in 2D and tetrahedra in 3D)
 301 using linear shape functions for both the velocity and pressure fields. The for-
 302 mulation is stabilized with the Finite Increment Calculus (FIC) technique [22,
 303 9,23]. In the FIC scheme for Lagrangian formulations [9], the stabilization
 304 terms are added to the continuity equation only. The derivation of the FIC-
 305 FEM stabilized form of the fluid governing equations is considered out of the
 306 scope of this work. Details can be found in [9]. In this section, only the final
 307 fully-discretized and linearized form is given.

308 The time step solution is obtained through an iterative two-step procedure
 309 where the linear momentum equations are solved for the increments of nodal
 310 velocities $\Delta \bar{\mathbf{v}}$ and the stabilized continuity equation is solved for the nodal
 311 pressures $\bar{\mathbf{p}}$.

Considering a generic time step $[{}^n t; {}^{n+1} t]$ of duration Δt (same time step
 used for the FEM solution of the solid mechanics problem), at each iteration
 k , the increment of nodal velocities are obtained from the discretized form of
 the linear momentum equations (Eq. (31)) as

$$(\mathbf{K}^p + \mathbf{K}^m) \Delta \bar{\mathbf{v}}_{k+1} = \mathbf{r}_k \quad (36)$$

with

$$\begin{aligned} \mathbf{K}_{IJ}^p &= \mathbf{I} \int_{\Omega} \frac{2\rho_f}{\Delta t} N_I N_J d\Omega, & \mathbf{K}_{IJ}^m &= \int_{\Omega} \mathbf{B}_I^T \mathbf{C} \mathbf{B}_J d\Omega \\ r_{Ii} &= \int_{\Omega} \rho_f N_I N_J d\Omega \bar{v}_{Ji} + \int_{\Omega} \frac{\partial N_I}{\partial x_j} \sigma_{ij} d\Omega - \int_{\Omega} \rho_f g_i N_I d\Omega \end{aligned} \quad (37)$$

where N_I is the linear shape functions for node I and matrices \mathbf{B} and \mathbf{C} are
 defined for a two dimensional problem as follows

$$\mathbf{B}_I = \begin{bmatrix} \frac{\partial N_I}{\partial x} & 0 \\ 0 & \frac{\partial N_I}{\partial y} \\ \frac{\partial N_I}{\partial y} & \frac{\partial N_I}{\partial x} \end{bmatrix}, \quad \mathbf{C} = \begin{bmatrix} \hat{\kappa}_f \Delta t + \frac{4\mu_f}{3} & \hat{\kappa}_f \Delta t - \frac{2\mu_f}{3} & 0 \\ \hat{\kappa}_f \Delta t - \frac{2\mu_f}{3} & \hat{\kappa}_f \Delta t + \frac{4\mu_f}{3} & 0 \\ 0 & 0 & \mu_f \end{bmatrix} \quad (38)$$

312 The pseudo-bulk modulus $\hat{\kappa}_f$ used in the fluid constitutive matrix \mathbf{C} is ob-
 313 tained by reducing *ad hoc* the real fluid bulk modulus κ_f to avoid ill-conditioning
 314 the algebraic linear system [10].

After solving solution of Eq. (36) and updating the fluid kinematic with the
 new velocities, the fluid nodal pressures $\bar{\mathbf{p}}$ are computed from the discretized
 FIC-stabilized form of the continuity equation (Eq. (32)) as follows

$$(\mathbf{M} + \mathbf{S}^T) \bar{\mathbf{p}}_{k+1} = \mathbf{M}^n \bar{\mathbf{p}} - \mathbf{Q}^T \bar{\mathbf{v}}_{k+1} + \mathbf{f}_{k+1}^r \quad (39)$$

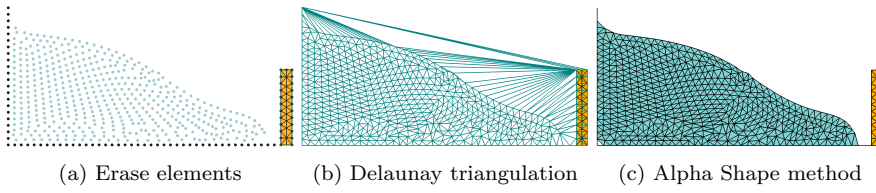


Fig. 3: PFEM remeshing steps. Not active fluid-structure interaction.

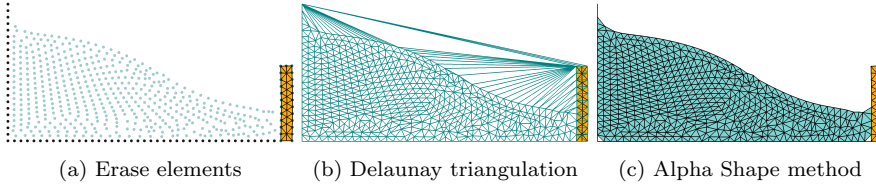


Fig. 4: PFEM remeshing steps. Active fluid-structure interaction.

with

$$M_{IJ} = \int_{\Omega} \frac{N_I N_J}{\kappa_f \Delta t} d\Omega, \quad \mathbf{Q}_{IJ} = \int_{\Omega} \mathbf{B}_I^T \mathbf{m} N_J d\Omega \quad (40)$$

315 where, for two dimensional problems, $\mathbf{m} = [1, 1, 0]^T$.

316 \mathbf{S}^r and \mathbf{f}^r are the stabilizing terms arising from the FIC method [9] and
317 are given in Appendix B.

318 Eq.(36) and Eq.(39) are solved iteratively within each fluid time step in-
319 crement until the fulfillment of the convergence criterion chosen.

320 3.3 Remeshing procedure with the PFEM

321 The fluid governing equations are solved using a Lagrangian mesh. For fluid dy-
322 namics problems, this strategy leads inevitably to a deterioration of the mesh
323 quality. This inconvenience is circumvented in the PFEM by building a new
324 discretization from the nodes of the previous mesh, whenever this mesh has ex-
325 ceeded a threshold level of distortion. The remeshing step of the PFEM is done
326 by combining Delaunay triangulation [12] and the Alpha Shape method [11].
327 Figs. 3 and 4 show graphically the PFEM remeshing steps for two different
328 situations of FSI analysis. In particular, Fig. 3 shows a time instant in which
329 the fluid and the solid domains are not interacting, whereas Fig. 4 represents
330 a situation in which the fluid-solid interaction is active.

331 As shown in Figs. 3a and 4a, the first step of PFEM remeshing consists of
332 erasing all the fluid elements of the previous distorted mesh. It is important
333 to note that the nodes of the previous mesh are preserved together with all
334 the problem information (nodal unknowns and physical parameters) and the
335 solid mesh is not affected by the PFEM remeshing.

336 In the second step of remeshing, the Delaunay triangulation is built over
 337 the cloud of points formed by the nodes of the previous mesh. As shown in Figs.
 338 3b and 4b, the Delaunay mesh is built also considering the nodes belonging to
 339 rigid contours and the boundary nodes of the solid domain (interface nodes).

340 In order to recognize the actual boundaries of the fluid domain (both the
 341 free surface and the new interface with the solid and rigid boundaries), the
 342 Alpha Shape method is applied. This technique evaluates the quality of all the
 343 elements created by the Delaunay triangulation and removes from the mesh
 344 those elements that exceed a limit value of distortion or size. In this way, the
 345 algorithm is capable to recognize the updated boundaries of the computational
 346 domain with good accuracy, as shown in Fig. 3c and 4c. This step is crucial
 347 to establish whether the fluid and the solid domains are in contact or not. In
 348 the positive case, the fluid and the solid solutions will be coupled, as in the
 349 situation described in Fig. 4. In the opposite case (Fig. 3), the fluid solution
 350 will not be affected by the solid one and vice versa, at least for the duration
 351 of the next time step increment.

352 It is important to remark that the fluid and the solid meshes must have a
 353 similar size at the interface zone to avoid topological inconveniences, such as
 354 non-physical fluid leakage or penetration into solid domains.

355 More details about the PFEM remeshing process and its implications can
 356 be found in [24, 7, 8].

357 The overall PFEM solution scheme for a generic time step $[{}^n t; {}^{n+1} t]$ of
 358 duration Δt is summarized in Algorithm 2.

Algorithm 2: PFEM solution algorithm for free-surface fluid solution and fluid-solid interface detection for a generic time step $[{}^n t; {}^{n+1} t]$ of duration Δt .

```

Initialization of the implicit transient dynamic scheme for the PFEM:
 $k \leftarrow 0$ ,  $\bar{\mathbf{v}}_0 \leftarrow {}^n \bar{\mathbf{v}}$ ,  $\bar{\mathbf{p}}_0 \leftarrow {}^n \bar{\mathbf{p}}$ 
while  $\frac{\|\Delta \bar{\mathbf{v}}_{k+1}\|}{\|\bar{\mathbf{v}}_0\|}$  and  $\frac{\|\bar{\mathbf{p}}_{k+1} - \bar{\mathbf{p}}_k\|}{\|\bar{\mathbf{p}}_0\|} > tolerance$  do
  | Compute the linear momentum equations for  $\Delta \bar{\mathbf{v}}_{k+1}$  (Eq. 36).
  | Update the kinematics:  $\bar{\mathbf{x}}_{k+1}, \bar{\mathbf{v}}_{k+1}, \bar{\mathbf{a}}_{k+1}$ .
  | Compute the continuity equation for  $\bar{\mathbf{p}}_{k+1}$  (Eq. 39).
  |  $k += 1$ 
end
if Mesh distortion  $> tolerance$  then
  | Erase the fluid elements and maintain the nodes (Figs. 3a and 4a).
  | Create Delaunay Triangulation over the cloud of nodes (Figs. 3b and 4b).
  | Do Alpha Shape check to recognize the free-surface boundaries and the
  | fluid-solid interface (Figs. 3c and 4c).
end

```

4 PFEM-FEM-DEM solution scheme for FSI

The FSI problem is solved by combining the FEM-DEM approach for solving non-linear solid mechanics problem (Section 2) and the PFEM to simulate the free-surface fluid flow and to detect the fluid-solid interface (Section 3.3).

The Lagrangian nature of PFEM and its efficient remeshing procedure allow for an easy transmission of boundary conditions between the fluid and the solid. Indeed, at the interface, the PFEM and the FEM-DEM nodes coincide and there is no need of using any projector operator to transfer the kinematics and/or the pressures between the different domains. As the fluid-solid interface may vary during the computation, either because the fluid free-surface has changed or because some new solid contours have been formed from crack propagation, this operation must be carried out continuously during the computation (in practice at each time step). Once the new fluid mesh has been built, the FSI time step is solved maintaining as fixed the connectivity of the elements.

The solution of the coupled problem is obtained with an iterative block Gauss-Seidel (BGS) procedure with Aitken relaxation.. At each iteration, the fluid dynamics problem is solved implicitly with the PFEM keeping fixed the velocity at the solid boundary. The fluid pressures obtained at the interface nodes are then transferred to the FEM-DEM as equivalent nodal forces $\mathbf{f}_{\text{fluid}}$ (Eq.(8)) and the solid mechanics solution is obtained. We remark that in problems where at the interface the fluid shear stress is significant with respect to the pressure value, the normal projection of the whole Cauchy stress tensor should be considered rather than the only fluid pressure. In the impact problems analyzed in this work, the fluid shear stress contribution has been considered as negligible for the FSI solution. In case of contact between two solids, also the equivalent nodal forces due to contact $\mathbf{f}_{\text{contact}}$ of Eq. (8) are computed using the DEM particles placed at the solid boundaries (Section 2.3).

To improve the convergence and stability of the FSI scheme, an Aitken relaxation technique is adopted, analogously to [5]. A schematic representation of the algorithm is shown in Fig. 5.

Following the Aitken method, at each iteration i of the coupled problem, the velocities obtained at the fluid-solid interface Γ_{fs} from the solid FEM solution ($\tilde{\mathbf{v}}_{\Gamma_{fs}}^{i+1}$), are transferred to the fluid interface nodes as an intermediate *relaxed* velocity $\mathbf{v}_{\Gamma_{fs}}^{i+1}$, computed as:

$$\mathbf{v}_{\Gamma_{fs}}^{i+1} = \omega^{i+1} \tilde{\mathbf{v}}_{\Gamma_{fs}}^{i+1} + (1 - \omega^{i+1}) \mathbf{v}_{\Gamma_{fs}}^i \quad (41)$$

where the Aitken relaxation parameter ω_i is computed as:

$$\omega^{i+1} = -\omega^i \frac{\mathbf{R}^{i+1^T} (\mathbf{R}^{i+1} - \mathbf{R}^i)}{\|\mathbf{R}^{i+1} - \mathbf{R}^i\|^2} \quad (42)$$

being $\mathbf{R}^i = \tilde{\mathbf{v}}_{\Gamma_{fs}}^i - \mathbf{v}_{\Gamma_{fs}}^i$.

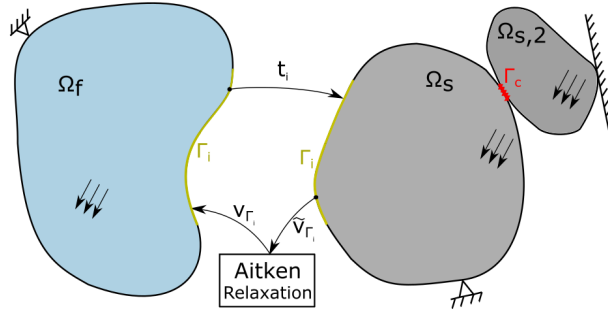


Fig. 5: Strong coupling between the fluid (Ω_f) and the solid (Ω_s) with the Aitken relaxation technique. Exchange of fluid tractions \mathbf{t} and relaxed solid velocities \mathbf{v} at the fluid-solid interface Γ_{fs} . Schematic representation of the contact between two solids in Γ_c .

397 In this work, the initial value of the Aitken parameter has been set to 0.825.

398 The iterative FSI loop concludes when the following converge criterion is
399 fulfilled:

$$\frac{\|\mathbf{R}^i\|}{\text{Number of DoF}} < tol, \quad (43)$$

400 Being tol a certain error tolerance, usually 10^{-5} m/s.

401 The FSI coupling method of the proposed PFEM-FEM-DEM approach is
402 summarized in Algorithm 3.

Algorithm 3: PFEM-FEM-DEM coupled solution scheme for a time step.

```

For each time step:
  Detect the new fluid-solid interface position with the PFEM (Section 3.3)
  while  $\|\mathbf{R}^i\| / \text{Number of DoF} > tol$  do
    Fix the velocity and position of the interface nodes of the solid.
    Solve the free-surface fluid flow with the PFEM (do Alg. 2)
    Free the velocities and position of the boundary nodes of the solid
    Update the values of the fluid pressure loads on the solid part (Eq. 6)
    Solve the FEM-DEM part of the calculation (do Alg. 1)
    Relax the interface nodal velocities via Aitken relaxation (Eq. 41)
    Check convergence of velocities at the interface  $\Gamma_i$  (Eq. 43)
  end

```

5 Numerical examples

Five numerical examples are presented to validate the proposed PFEM-FEM-DEM formulation and to highlight specific features of the method. The first example shows the capacity of the formulation to deal with submerging solid objects in a free-surface fluid. In the second example, the accuracy of the FSI method for the solution of impacts of fluids against deformable structures is proved by analyzing a benchmark test for FSI problems in presence of free-surface flows and large displacements of the solid structure. The same problem is then solved modifying the material parameters in order to allow the fracture and breakage of the solid. Next, the progressive collapse of a 3D solid slab due to the accumulation of a free-surface fluid is reproduced. Finally, the structural failure of a concrete wall under the action of a tsunami wave is presented.

5.1 Wedge water entry

This first test has been chosen to show the capability of the method to simulate the interaction between free solid debris and a free-surface fluid. A situation that may occur after the desegregation of a structure. The experimental test used as reference is the one presented in [40]. In the experiment, a solid wedge was made falling on a tank filled with water from an initial height of 1.3 m. Here, the two-dimensional adaptation of the experimental test is presented. The initial geometry of the example is depicted in Fig. 6. The material properties used are defined in Table 1. To reproduce the rigid behavior of the solid observed in the experiment, a very high value for the Young modulus of the solid has been used. The analysis has been run using a fixed time step duration of 10^{-4} s.

The solid domain has been discretized with 5,833 3-nodded triangles whereas the fluid domain with 65,586 ones. We used for the solid mesh the same (small) size as the fluid one to enable the formation of the conforming mesh at the interface and to capture more accurately the timing of the impact of the wedge on the fluid at rest (see Section 3.3).

The numerical results have been compared to the experimental observations of [40] and to the numerical results obtained by the monolithic PFEM formulation [42] and the SPH method [41].

In Fig. 7 the numerical results obtained at four different time steps are shown. The pictures show the impact of the wedge against the water at rest. The edge almost maintains the initial inclination and penetrates into the water without rotating. On the other hand, two symmetric streams of water depart laterally due to the impact of the solid object. Fig. 8 shows the time evolution of the obtained velocity of the wedge and the experimental solution. After an initial free-fall regime, the wedge decelerates progressively from a peak velocity of around 5 m/s. To better appreciate the wedge deceleration phase, Fig. 9 shows the velocity evolution of the solid after the impact against the fluid.

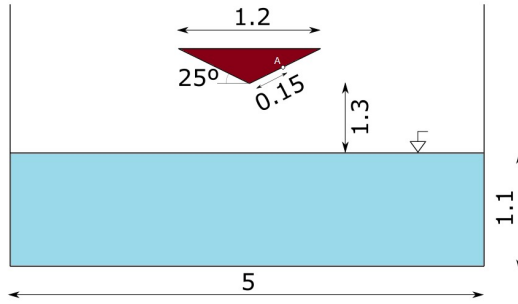


Fig. 6: Initial setup of the wedge water entry problem. Units in m .

Parameter	Value
Solid Young's modulus (E)	10 GPa
Solid Poisson's ratio (ν)	0.0
Solid Density (ρ_s)	466.07 kg/m^3
Fluid Viscosity (μ)	0.001 $Pa \cdot s$
Fluid Density (ρ_f)	1000 kg/m^3

Table 1: Wedge water entry. Material data.

444 For the same time interval, Fig. 10 also shows the time evolution of pressure
 445 measured at point A of the wedge. The graphs show that all the numerical
 446 methods capture very well the first pressure peak measured in the laboratory
 447 test. However, after that, the numerical results generally underestimate the
 448 pressure values obtained experimentally. It can be speculated that this slight
 449 discrepancy may be due to the plain strain hypothesis assumed in all the
 450 numerical simulations.

451 Figs. 9-10 shows a very good agreement between the results of the proposed
 452 PFEM-FEM-DEM method and the numerical and experimental results of the
 453 literature proving the accuracy of the method in the simulation of inertially
 454 driven FSI problems.

455 5.2 Dam break against a flexible wall

456 The collapse of a water column against an elastic membrane is a well-known
 457 benchmark for FSI problems with free-surface fluids. The test was initially
 458 proposed by Walhorn et al. [37] and later reproduced in several other works,
 459 some others using the PFEM [34, 32, 5], which are here taken as reference. The
 460 initial setup of the example is shown in Fig. 11. The material properties and
 461 the geometry data are given in Table 2. For the solid, a Neo-Hookean large
 462 strain constitutive law has been used. The initial meshes used for the solid and
 463 the fluid solutions are composed of 2,437 and 3,766 linear triangular elements,
 464 respectively.

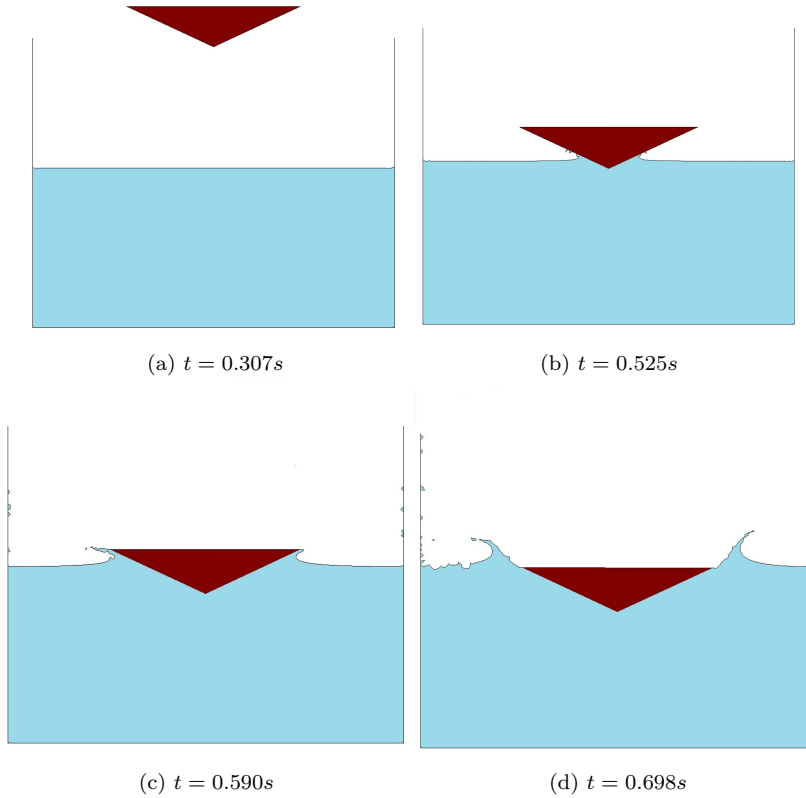


Fig. 7: Wedge water entry. Numerical results at four time instants.

465 Regarding the problem data, the time step used is $\Delta t = 1e-3s$, the re-
 466 laxation procedure used is the Aitken methodology with a tolerance of $1e-5$
 467 $m/(s \cdot DoF)$ and a maximum relaxation of ω_{max} of 0.9.

468 The horizontal displacement of the elastic obstacle is tracked along time
 469 meanwhile is being hit by the fluid column.

470 Fig. 13 shows some representative snapshots of the numerical simulation.

471 Fig. 12 plots the time evolution of the horizontal displacement of the left
 472 top corner of the solid membrane. The graph shows an overall good agreement
 473 with the results of the literature [34,32,5].

474 We note that all the numerical results are almost coincident in the first 0.5s
 475 of simulation. After this time period, some discrepancy appears. Nevertheless,
 476 this can be considered as unavoidable due to the high unsteadiness exhibited
 477 by the fluid flow in this test.

478 Globally, the good results of this validation test confirm the suitability of
 479 the proposed method for FSI problems in presence of large displacements and
 480 deformation of both the fluid and the solid domains.

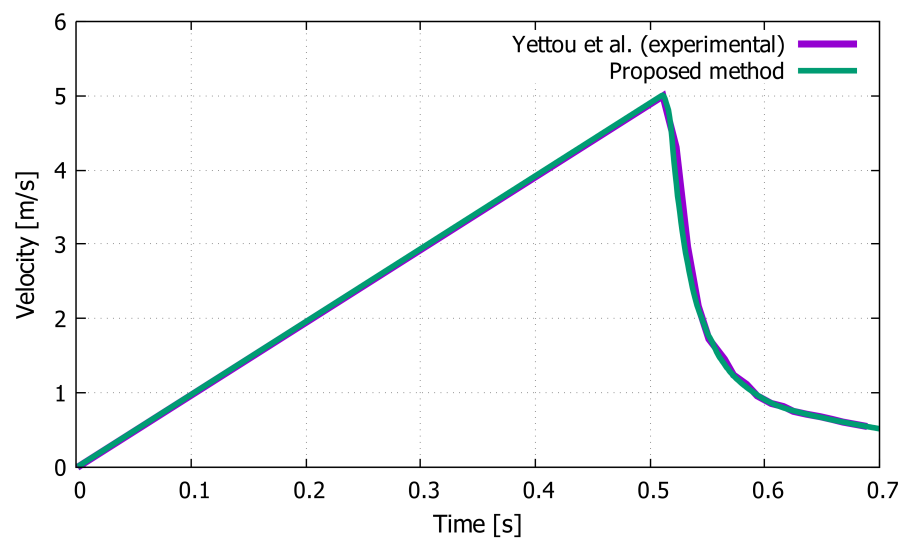


Fig. 8: Time evolution of the vertical velocity of the wedge. Comparison between the results obtained in this work and the experimental one [40].

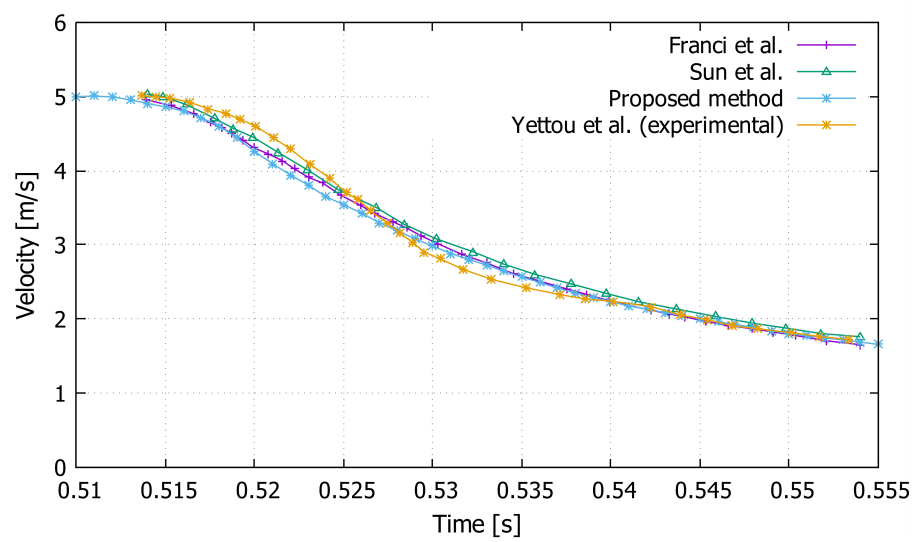


Fig. 9: Time evolution of the vertical velocity of the wedge. Comparison between the results obtained in this work and those of Sun et al. [41], Franci et al. [42] and Yettou et al. [40].

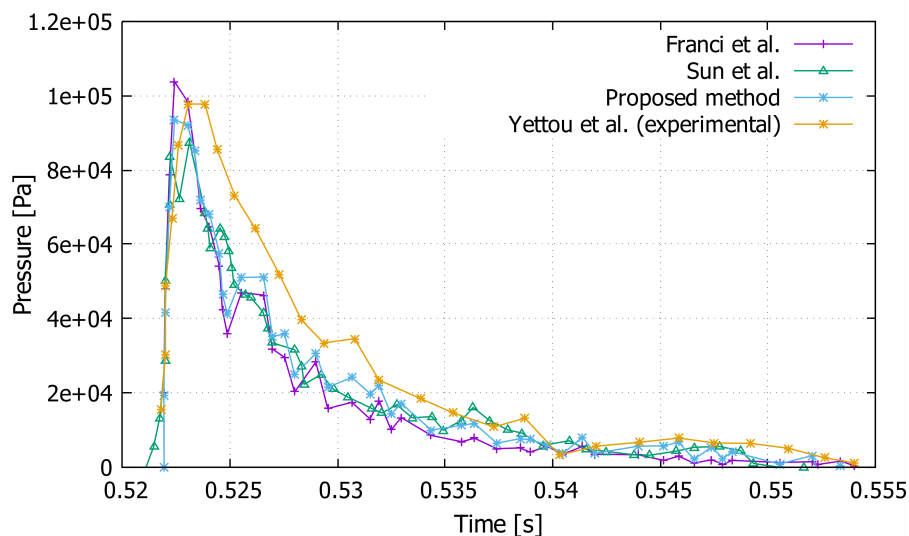


Fig. 10: Time evolution of the fluid pressure at point A of the wedge. Comparison between the results obtained in this work and those of Sun et al. [41], Franci et al. [42] and Yettou et al. [40].

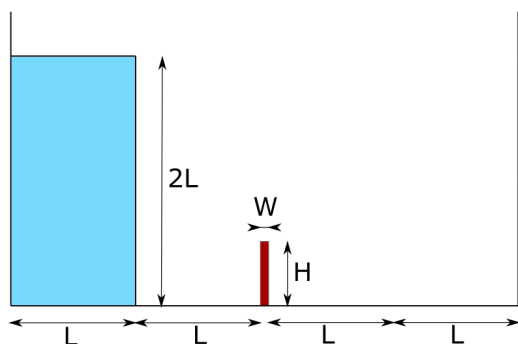


Fig. 11: Initial setup of the dam break against a flexible wall.

481 5.3 Dam break against a fracturing wall

482 Here, the same test studied in Section 5.2 is analyzed changing the material
 483 properties of the solid in order to allow the breakage of the solid wall. The
 484 material properties are provided in Table 3. The solid membrane is much stiffer
 485 than the previous one and more similar to a concrete structure. An initial
 486 layer of discrete elements has been placed at the contour of the solid body to
 487 prevent the indentation between the detached wall and the ground/walls of

Parameter	Value
Solid Young's modulus (E)	1.0 MPa
Solid Poisson's ratio (ν)	0.0
Solid Density (ρ_s)	2500 kg/m ³
Fluid Viscosity (μ)	0.001 Pa · s
Fluid Density (ρ_f)	1000 kg/m ³
L	0.146 m
H	0.080 m
W	0.012 m
Gravity	9.81 m/s ²

Table 2: Problem data for the dam break against a flexible wall.

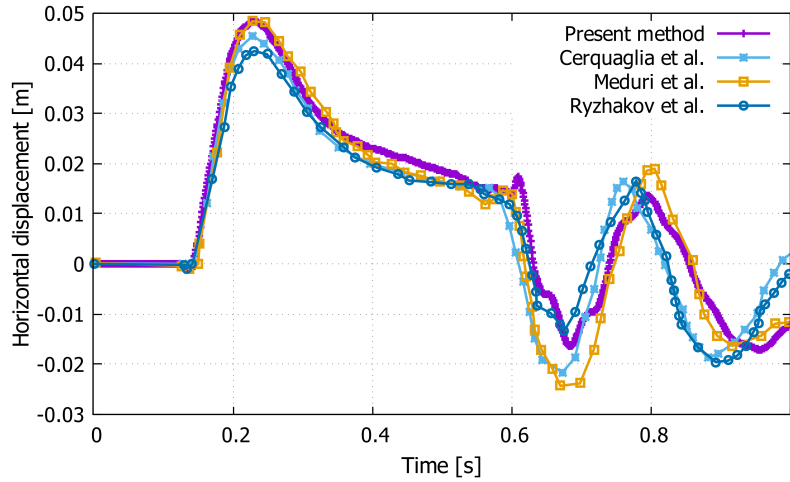


Fig. 12: Evolution of the horizontal displacement of the tip of the wall along time.

488 the geometry. In this case, a lower time step was used ($\Delta t = 1e-4s$) to describe
 489 properly the violent fluid-solid and solid-solid interactions.

490 As shown in Fig. 14, the impact of the water on the wall induces a crack at
 491 its base. Once fully detached, the solid structure is dragged by the fluid flow
 492 and impacts against the containment walls.

493 Fig. 15 shows the error value computed using Eq.(43) for each Aitken
 494 iteration and at two time steps, namely $t = 0.296s$ and $t = 0.326s$. Both time
 495 instants refer to the post-failure scenario, so to the most unsteady phase of
 496 the analysis. In both graphs, a clear linear convergence rate of the Aitken
 497 iterations is obtained.

498 Additionally, this example has been calculated using three different time
 499 steps: 10^{-4} , 10^{-5} and $5 \cdot 10^{-6}s$, obtaining very stable results as can be see in
 500 Fig. 16.

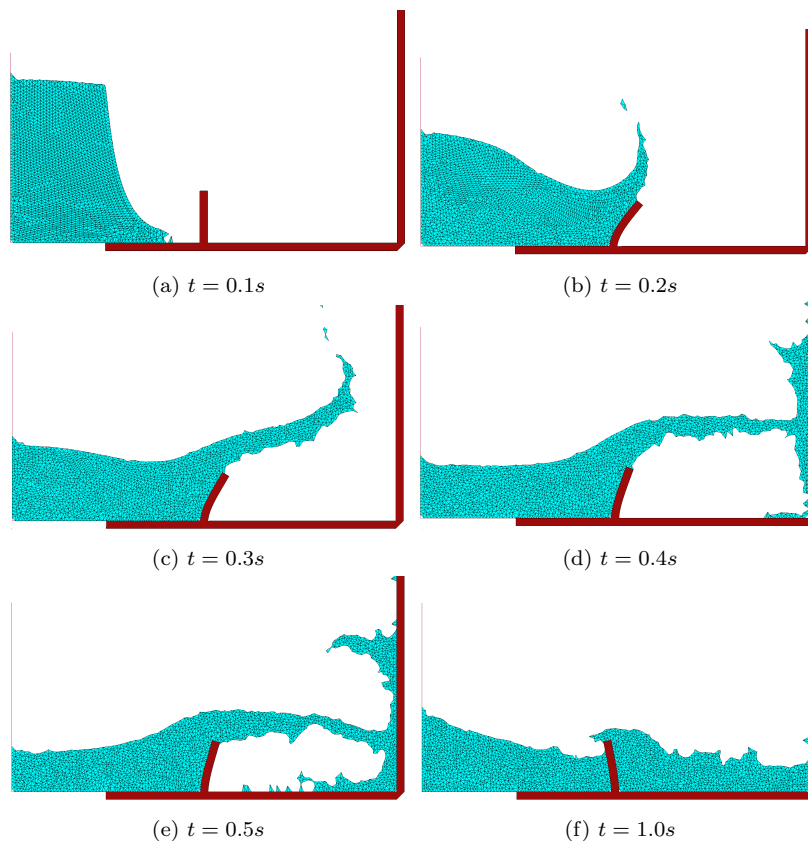


Fig. 13: Time lapse of the water impacting over a flexible wall.

501 Finally, this example has been reproduced using four different FE meshes
 502 (3722, 9694, 35,980 and 135,270 DoF). The fractured geometries are depicted
 503 in Fig. 17. As expected, the crack is located at the lower part of the vertical
 504 wall in all cases. The horizontal displacement of the upper end of the wall
 505 can be seen in Fig. 18. Additionally, in Fig. 19, a convergence analysis of the
 506 horizontal displacement of the wall at $t = 0.2s$ is plotted. One can see how the
 507 solution converges to the most accurate result (fine mesh) as long as we use
 508 meshes with a greater number of DoF.

509 5.4 3D slab collapse due to fluid weight

510 The present example consists of simulating the failure of a slab with a central
 511 notch due to the weight of a fluid flow that accumulates on top of it. The inlet
 512 used for the fluid is inclined 45 degrees and has been positioned in the middle
 513 of the slab section (in $z - y$ plane) in order to recreate a full three-dimensional
 514 problem. The inlet lower edge is located at 0.86 m above the slab upper level.

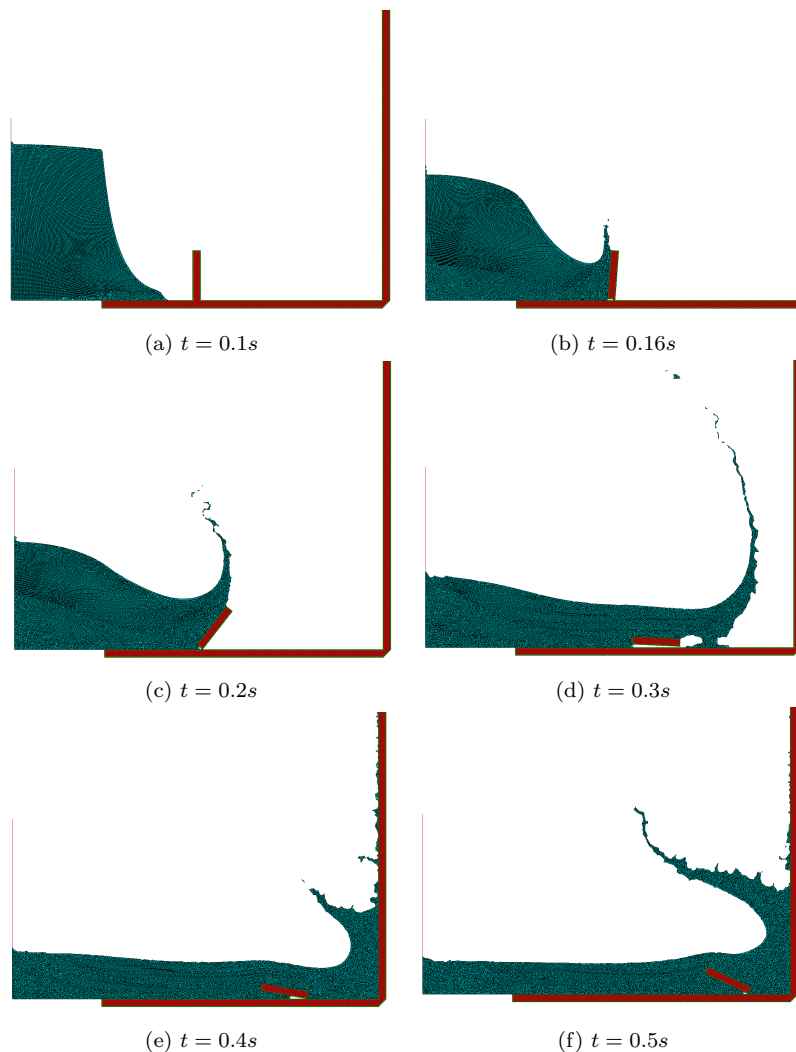


Fig. 14: Time evolution of the water impacting over a fracturing wall.

515 The solid slab has an initial imperfection - an artificial notch with height 0.1
 516 m and width 0.01 m - that will propitiate the onset of the crack at the central
 517 part of the structure. The slab is fixed in the upper axis that is aligned with
 518 the initial notch.

519 The geometry of the problem is depicted in Fig. 20. The material properties
 520 used for the solid and the fluid domains are given in Table. 4. The yield
 521 surface used in the solid part is Rankine. A Newtonian fluid with high viscosity
 522 ($\mu = 100Pa \cdot s$) and density ($\rho_f = 2400kg/m^3$) has been considered. The time

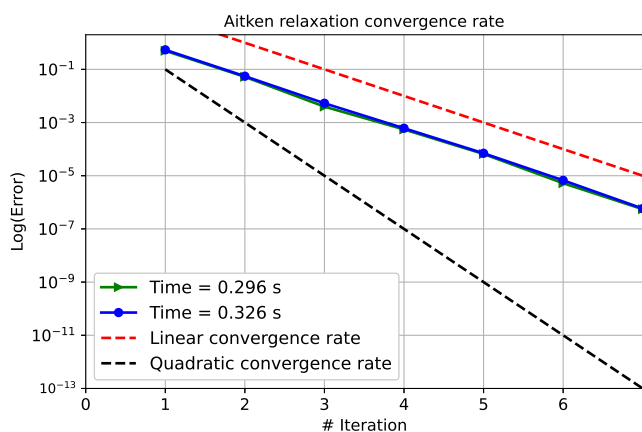


Fig. 15: Aitken convergence rate for different time steps.

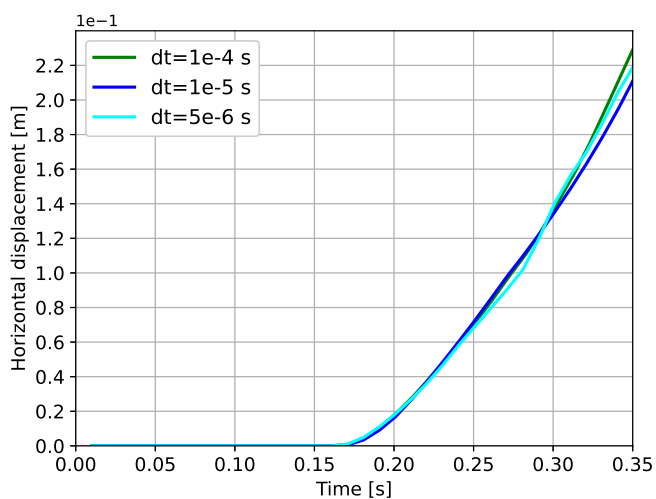


Fig. 16: Comparison of the computed horizontal displacement of the wall for different time steps.

523 step used ranges between $\Delta t = 10^{-3}$ - 10^{-4} s depending on the stage of the
 524 calculation. The Aitken velocity tolerance is $10^{-5} \text{ m}/(\text{s} \cdot \text{DoF})$.

525 Fig. 21 shows the time evolution of the collapse of the concrete slab. The
 526 fluid accumulates on the top of the concrete slab and fills progressively the con-
 527 tainment until the maximum strength capacity of the solid is reached (around
 528 $t \approx 1.9$ s). Then, as expected, the crack is generated at the central notch

Parameter	Value
Solid Young's modulus (E)	30 GPa
Solid Poisson's ratio (ν)	0.0
Solid Density (ρ_s)	2400 kg/m^3
Solid tensile strength (f_t)	0.5e5 Pa
Solid Fracture energy (G_f)	10 J/m^2
Fluid Viscosity (μ)	0.001 Pa · s
Fluid Density (ρ_f)	1000 kg/m^3
L	0.079 m
H	0.14 m
A	0.1 m
s	0.005 m

Table 3: Problem data for the dam break against a fracturing wall.

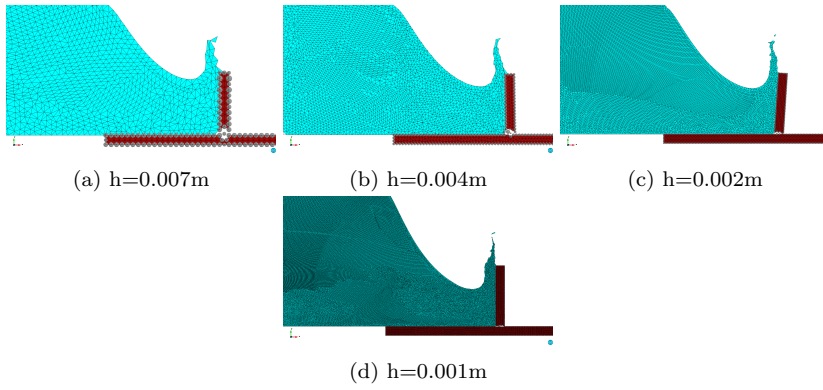


Fig. 17: Fractured geometry for different FE mesh sizes.

529 and it propagates vertically through the thickness of the slab and for all its
530 length ($t \approx 2$ s). As shown in Fig. 21, a set of DEM particles is introduced
531 on the fracture labels to avoid mutual solid penetration. Once the continuity
532 of the solid structure is broken by the propagated fracture, the two parts of
533 the slab start moving independently rotating around the z axis aligned with
534 their clamped edges. The fluid is then free to flow downwards due to gravity.
535 The final number of finite elements used for the fluid part is 52,738 linear
536 tetrahedral elements.

537 5.5 Failure of a concrete wall due to a tsunami force

538 This numerical test aims to model the failure of a concrete structure subjected
539 to a tsunami-type impulse force. The problem is inspired by the experimental
540 tests conducted by Arikawa et al. [67] in a 184m long channel. In the experi-
541 mental test, the tsunami wave was produced through a piston-type wave maker
542 capable of generating a maximum wave 3.5 m height. The concrete plate was
543 clamped at its lateral sides over two concrete columns, while the upper and

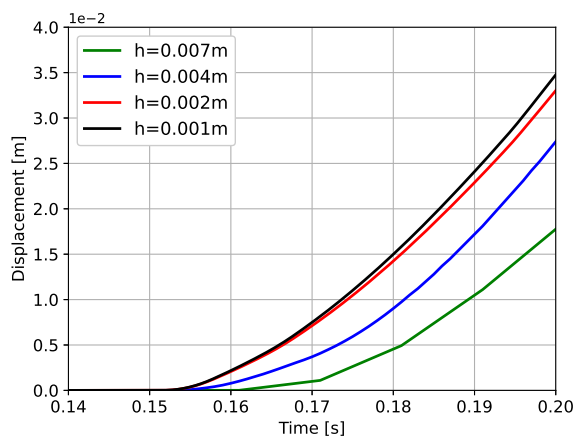


Fig. 18: Time evolution of the horizontal displacement for different FE mesh sizes.

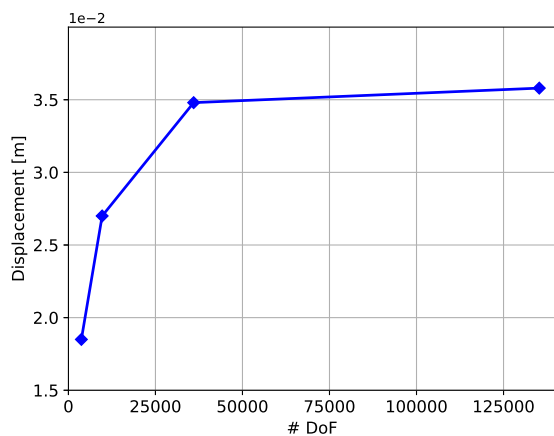
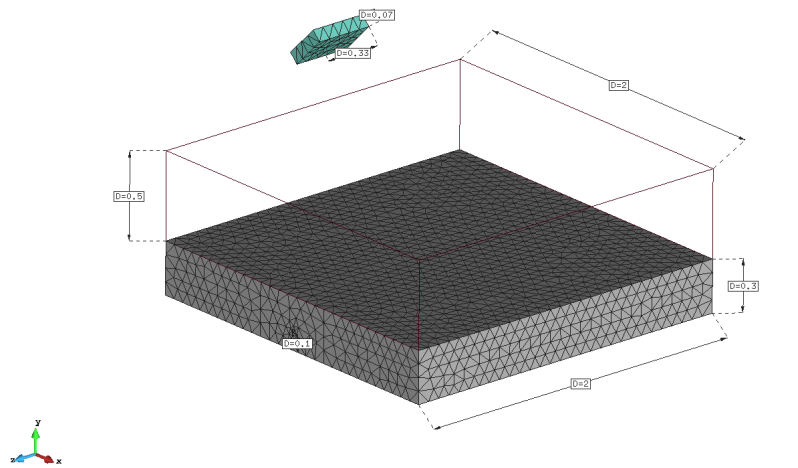


Fig. 19: Horizontal displacement obtained for different FE discretizations at $t = 0.2s$.

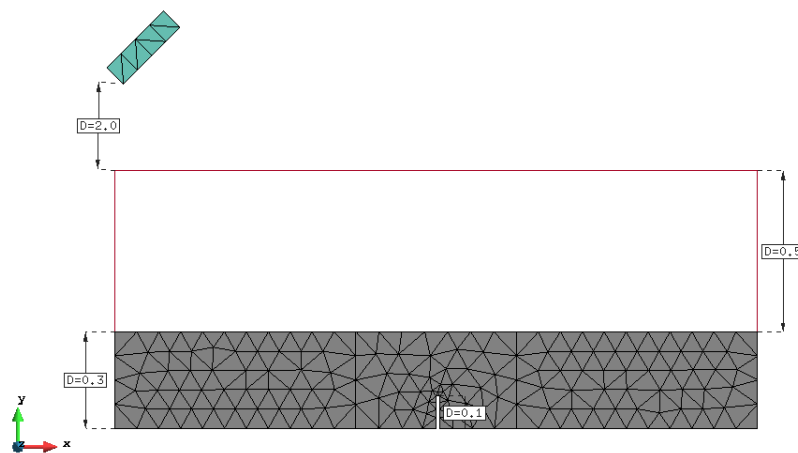
544 lower sides were free to move. The geometry of the wall, its boundary conditions
 545 and the material parameters (Table 5) here considered are the same as
 546 in [67]. In the experiments, the concrete wall was also provided with a thin
 547 steel mesh that has not been taken into account in this numerical simulation.
 548 In future works, it is planned to consider also the effect of reinforcement steel
 549 bars in concrete structures by using, for instance, a phenomenological rules of

Parameter	Value
Solid Young's modulus (E)	35 GPa
Solid Poisson's ratio (ν)	0.2
Solid Density (ρ_s)	2400 kg/m ³
Solid tensile strength (f_t)	0.5e6 Pa
Solid Fracture energy (G_f)	100 J/m ²
Fluid Viscosity (μ)	100 Pa · s
Fluid Density (ρ_f)	2400 kg/m ³

Table 4: Problem data for the 3D slab collapse example.



(a) Dimensions [m]



(b) FE mesh. Solid: 35,690 FE, Fluid: 153 FE.

Fig. 20: Initial geometry of the problem.

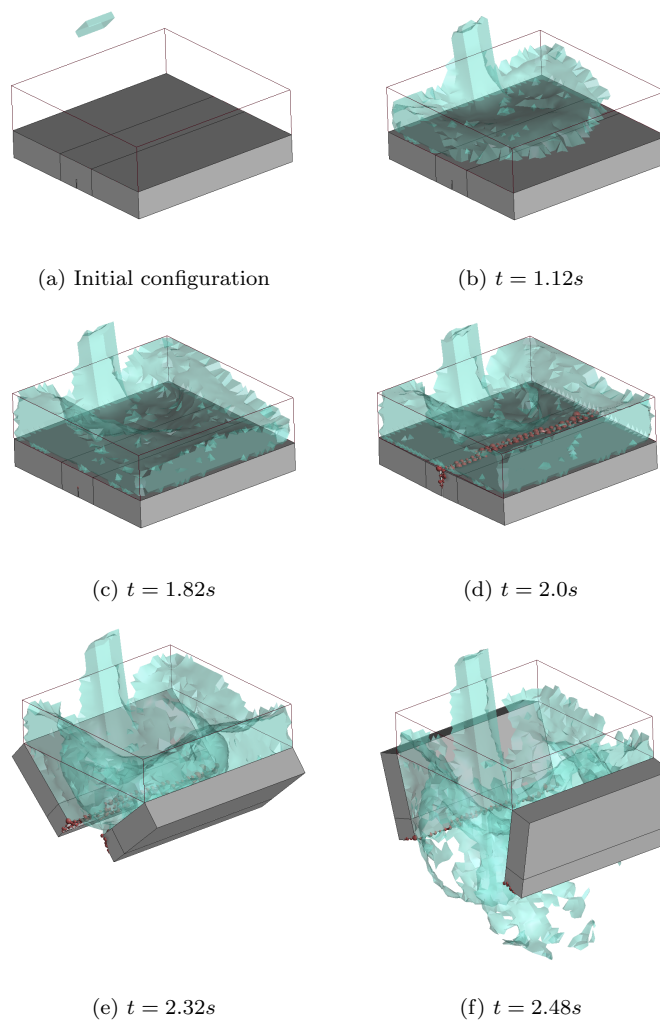


Fig. 21: Time evolution of the collapse of the structure.

550 mixtures, such as those employed in [68][69][70]. However, this is considered
 551 out of the scope of the present work.

552 Furthermore, to limit the high computational cost of the fully 3D model,
 553 only a reduced geometry of the channel is here analyzed, and the water wave is
 554 reproduced in an approximate way via an inlet condition applied to the water
 555 volume. The inlet velocity has been taken equal to $2m/s$, which was the peak
 556 value of the velocity measured experimentally at the impact zone.

557 Fig. 22 shows the FE mesh used for the fluid and the solid body and some
 558 useful distances. At the beginning of the analysis, the fluid and solid linear

Parameter	Value
Solid Young's modulus (E)	21 GPa
Solid Poisson's ratio (ν)	0.2
Solid Density (ρ_s)	2400 kg/m^3
Solid tensile strength (f_t)	3e6 Pa
Solid Fracture energy (G_f)	100 J/m^2
Fluid Viscosity (μ)	0.001 $Pa \cdot s$
Fluid Density (ρ_f)	1000 kg/m^3

Table 5: Problem data for the failure of a concrete wall under tsunami force.

559 tetrahedral elements are 17,275 and 37,359, respectively, and a structured mesh
560 has been used for the solid domain.

561 An adaptive time step has been used, ranging from $\Delta t = 2 \cdot 10^{-3} s$ to
562 $\Delta t = 10^{-4} s$, in order to better capture the cracking of the wall while reducing
563 the computational cost. The velocity tolerance used for the Aitken relaxation
564 is $10^{-4} m/(s \cdot DoF)$.

565 Fig. 23 shows some representative results of the analysis. To better ap-
566 preciate the fluid motion, also the velocity vectors are plotted over the fluid
567 domain. The pictures show how the fluid advances through the channel until
568 it hits the concrete wall (Fig. 23.d). The impulsive force produced by the fluid
569 impact induces the sudden failure of the lower part of the solid plate which
570 detaches from the rest of the structure. As it can be appreciated from Fig.
571 23.d, a main crack propagates straightly in the horizontal direction in the cen-
572 tral part of the wall. It should be noted that the almost perfect alignment of
573 the crack with the horizontal plane is, in part, a consequence of the use of a
574 structured mesh for the solid domain. In the case of using a not structured
575 mesh, although the general path of the fracture should be maintained, a cer-
576 tain misalignment with respect to the horizontal direction is expected to be
577 obtained.

578 This main horizontal crack intersects with the two vertical fissures placed
579 near the lateral constraints of the concrete wall, inducing the breakage and
580 release of the lower portion of the wall. This rectangular solid debris is then
581 pushed and dragged by the water flow that can now freely pass through the
582 holed solid structure (Fig. 23.e-23.f).

583 Fig. 24 shows, from two different perspectives, detailed views of the frac-
584 tured geometry of the concrete wall.

585 The resulting collapse mechanism of the wall is a punching-shear mode.
586 This is in agreement with the experimental data provided by Arikawa et al.
587 [67]. The fractured geometry of the wall obtained in the experiment is shown
588 in Fig. 25.

589 Despite the simplifications assumed in this analysis, this 3D test shows
590 the high potential of the proposed formulation for predicting and analyzing
591 the damages of real structures under the impact of natural hazards, such as
592 tsunami or floods.

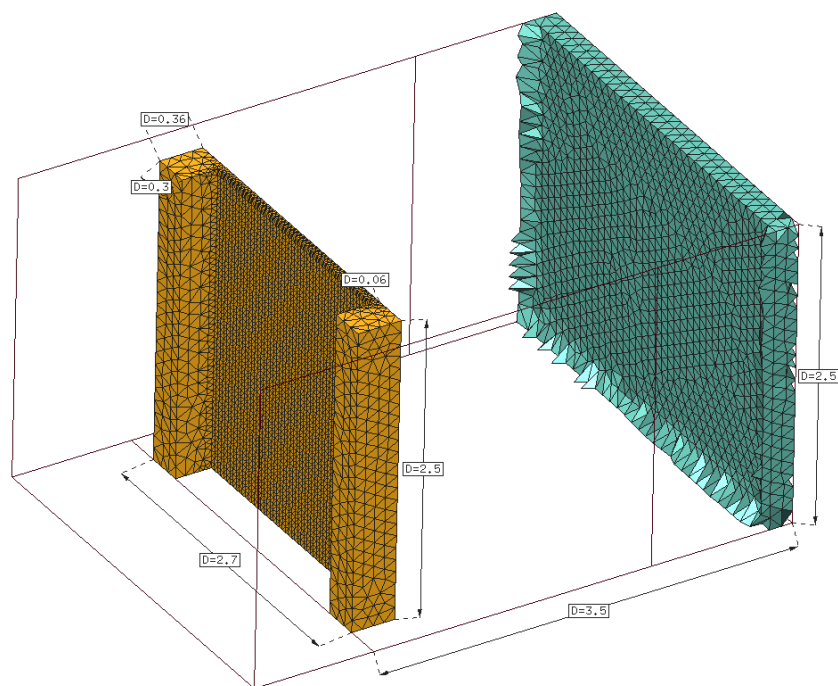


Fig. 22: Problem geometry and FE mesh. Solid: 37359 elements, Fluid: 17275 elements.

593 6 Conclusions

594 We have presented a coupled Lagrangian method for the simulation of FSI
 595 problems in presence of free-surface flows and fracturing solids.

596 The formulation uses the PFEM to solve the free-surface fluid dynam-
 597 ics problem and to detect the fluid-solid interface, and a coupled FEM-DEM
 598 method to model crack formation and propagation in structures and the con-
 599 tact interaction between different solids. An iterative staggered scheme with
 600 Aitken relaxation is used to guarantee a strong coupling of the FSI problem
 601 and to avoid numerical inconveniences, such as the ill-conditioning of the linear
 602 system or added-mass effects. The numerical method presented has demon-
 603 strated its potential to estimate damages on civil constructions due to natural
 604 hazards like floods, tsunamis, landslides, or explosions.

605 Several academic examples have been presented to validate the proposed
 606 technology in the framework of FSI problems with fracture phenomena. The
 607 numerical tests have shown that the method can reproduce the dynamics of a
 608 solid object in the water, to solve accurately FSI problems with strong fluid
 609 impacts and large solid displacements, to model crack formation due to fluid

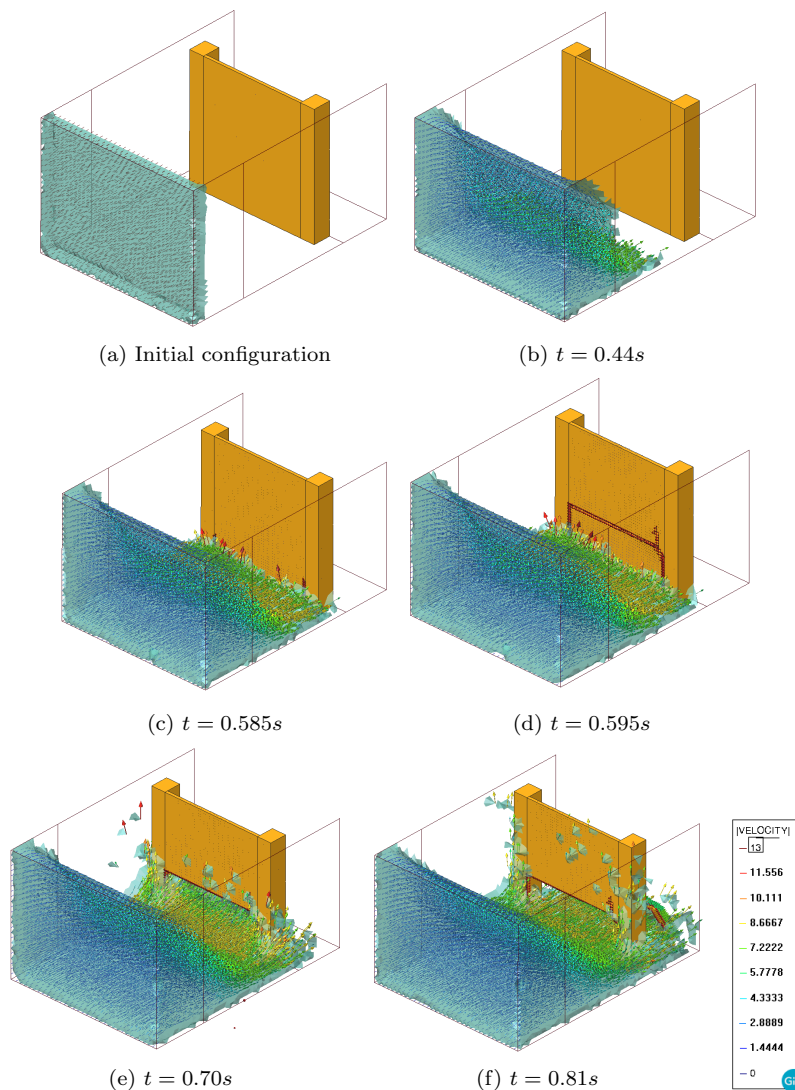


Fig. 23: Concrete wall under tsunami force. Velocity vectorial field of the fluid domain and cracked geometry of the structure.

610 hydrodynamic forces and its propagation in the structure, and to deal with
 611 solid fragmentation and multi-body contact interaction.

612 Finally, two 3D tests have been presented to show the potential of the
 613 proposed formulation for predicting the damages on real structures caused
 614 by the impact of free-surface fluids. In the first test, the failure of a plate
 615 is induced by the accumulation of a viscous fluid on its upper surface, while

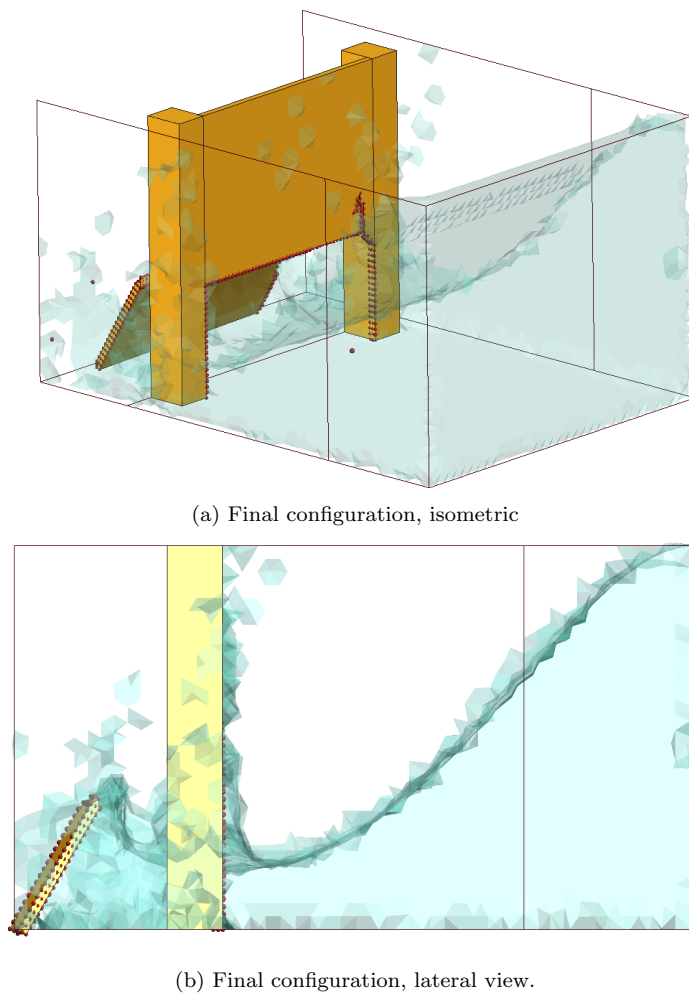


Fig. 24: Concrete wall under tsunami force. Fractured geometry of the wall.

616 in the second one, a concrete plate is made collapsing under the effect of an
 617 impulsive force produced by the impact of a tsunami-type wave.

618 Several future developments are planned to be considered to widen the ap-
 619 plication field of the proposed FSI method and to improve its computational
 620 performance. These include the use of adaptive remeshing algorithm to sim-
 621 ulate phenomena of crack formation and propagation in an optimized way,
 622 the implementation of new damage models and failure criteria for different
 623 materials than concrete, and the modeling of steel bars to simulate reinforced
 624 concrete structures.



Fig. 25: Concrete wall under tsunami force. Cracked geometry of the wall after the experiment conducted in Arikawa et al. [67].

625 A Tensors used for the FEM solution of solid mechanics problem

626 In this appendix, the variables and tensors introduced in Eqs. (8)-(9) are defined.

627 The matrices and vectors of Eq. (8) are computed as:

$$M_{KJ} = \int_{\Omega_0} \rho_0 N_{KI} N_{IJ} dV_0, \quad (44)$$

$$\mathbf{f}_{ext,K} = \int_{\partial\Omega_0} t_I N_{IK} dS_0 + \int_{\Omega_0} \rho_0 b_I N_{IK} dV_0 \quad (45)$$

$$\mathbf{f}_{int,K} = \int_{\Omega_0} S_{IJ} \nabla_I^S N_{JK} dV_0 \quad (46)$$

$$\mathbf{C} = \alpha_{\text{Ray}} \mathbf{M} + \beta_{\text{Ray}} \mathbf{K}_0 \quad (47)$$

628 Where N are the linear shape functions and parameters $\alpha_{\text{Ray}} = 0.5$ and $\beta_{\text{Ray}} = 0.02$
 629 are the standard Rayleigh coefficients for obtaining the damping matrix if some damping is
 630 considered, otherwise we set these values to zero, and \mathbf{K}_0 is the initial stiffness matrix.

631 In Eq. 9, $\mathbf{K}_T(\bar{\mathbf{u}}_k)$ is the tangential stiffness matrix, whose relationship with the internal
 632 forces \mathbf{f}_{int} is:

$$\mathbf{K}_T(\bar{\mathbf{u}}_k) = \frac{\partial \mathbf{f}_{\text{int}}(\bar{\mathbf{u}}_k)}{\partial (\bar{\mathbf{u}}_k)}. \quad (48)$$

633 In general, the tangential stiffness matrix $\mathbf{K}_T(\bar{\mathbf{u}}_k)$ depends on the tangent constitutive
 634 tensor \mathcal{C}_T whose numerical derivation can be found in [3]. This numerical procedure consists
 635 in obtaining an approximation of the tangent constitutive tensor \mathcal{C}_T by using finite differ-
 636 ences. For the j th column of the tangent constitutive tensor (depending if one uses forward
 637 or central differences) in small strains reads:

$$\mathcal{C}_{T,j} \simeq \frac{\boldsymbol{\sigma}(\boldsymbol{\varepsilon} + \delta\boldsymbol{\varepsilon}_j) - \boldsymbol{\sigma}(\boldsymbol{\varepsilon})}{\delta\varepsilon_j} \quad \text{or} \quad \mathcal{C}_{T,j} \simeq \frac{\boldsymbol{\sigma}(\boldsymbol{\varepsilon} + \delta\boldsymbol{\varepsilon}_j) - \boldsymbol{\sigma}(\boldsymbol{\varepsilon} - \delta\boldsymbol{\varepsilon}_j)}{2\delta\varepsilon_j} \quad (49)$$

638 where $\delta\boldsymbol{\varepsilon}_j$ is a zero vector except for the j th component whose value is a strain pertur-
 639 bation $\delta\varepsilon_j$, $\boldsymbol{\sigma}$ and $\boldsymbol{\varepsilon}$ are a measure of stresses and strains, respectively.

640 B FIC stabilization terms used for the PFEM solution

641 Here, the FIC terms used for the fluid problem stabilization and introduced in Section 3.2
 642 are detailed. The stabilization terms of the FIC technique [9] affect the continuity equation
 643 (Eq.(39)) only.

644 In Eq.(39), the FIC stabilization terms \mathbf{S}^τ and \mathbf{f}^τ are computed as [9]

$$\mathbf{S}^\tau = \left(\frac{1}{\Delta t^2} \mathbf{M}^c + \mathbf{L} + \mathbf{M}^b \right) \quad (50)$$

$$\mathbf{f}^\tau = \frac{\mathbf{M}^c}{\Delta t^2} ({}^n \bar{\mathbf{p}} + {}^n \dot{\bar{\mathbf{p}}} \Delta t) + \mathbf{f}^p \quad (51)$$

645 with

$$\begin{aligned} M_{IJ}^c &= \int_{\Omega} \tau \frac{\rho_f}{\kappa_f} N_I N_J d\Omega, \\ L_{IJ} &= \int_{\Omega} \tau (\nabla^T N_I) \nabla N_J d\Omega, \\ M_{IJ}^b &= \int_{\Gamma_t} \frac{2\tau}{h_n} N_I N_J, \\ f_I^p &= \int_{\Gamma_t} \tau N_I \left[\rho_f \frac{Dv_n}{Dt} - \frac{2}{h_n} (2\mu_f d_n - \hat{t}) \right] d\Gamma - \int_{\Omega} \tau \nabla^T N_I \rho_f \mathbf{g} d\Omega \end{aligned} \quad (52)$$

where Γ_t is the free-surface contour and the stabilization parameter τ is defined as

$$\tau = \left(\frac{8\mu_f}{h^2} + \frac{2\rho_f}{\delta} \right)^{-1} \quad (53)$$

646 where h and δ are characteristic distances in space and time. Details about the derivation
 647 of the stabilization terms can be found in [9].

648 **Acknowledgements** This research was supported by the Spanish Government through the
 649 FPU 16/02697 grant and by the Spanish Ministry of Economy and Competitiveness (Minis-
 650 terio de Economía y Competitividad, MINECO) through the Severo Ochoa Programme for
 651 Centres of Excellence in RD (CEX2018-000797-S), the project PRECISE (BIA2017- 83805-
 652 R) and the PARAFUID talk. The authors gratefully acknowledge the received support.

653 Conflict of interest

654 The authors declare that they have no conflict of interest.

References

- 656 1. Zárate F. and Oñate E., A simple FEM-DEM technique for fracture prediction in materials and structures, *Computational particle mechanics*, 2, page 301-314 (2015)
- 657 2. Zárate F., Cornejo A. and Oñate E., A three-dimensional FEM-DEM technique for predicting the evolution of fracture in geomaterials and concrete, *Computational particle mechanics*, 5, 411-420 (2018)
- 658 3. Cornejo A., Mataix V., Zárate F. and Oñate E., Combination of an adaptive remeshing technique with a coupled FEM-DEM approach for analysis of crack propagation problems, *Computational particle mechanics*, 1-18 (2019)
- 659 4. Zienkiewicz O.C., Zhu J.Z., The superconvergent patch recovery (SPR) and adaptive finite element refinement, *Comput Methods Appl Mech Eng*, 101, 207-224 (1992)
- 660 5. Cerquaglia M.L. and Thomas D. and Boman R. and Terrapon V. and Ponthot J.P., A fully partitioned Lagrangian framework for FSI problems characterized by free surfaces, large solid deformations and displacements, and strong added-mass effects, *Comput Methods Appl Mech Eng*, 348, 409-442 (2019)
- 661 6. Franci A. and Oñate E. and Carbonell J.M., Unified Lagrangian Formulation for solid and fluid mechanics and FSI problems, *Comput Methods Appl Mech Eng*, 298, 520-547 (2016)
- 662 7. Oñate E. and Idelsohn S. and Del Pin F. and Aubry R., The Particle Finite Element Method. An overview, *International Journal of Computational Methods*, 1, 267-307 (2004)
- 663 8. Franci A. and Cremonesi M., On the effect of standard PFEM remeshing on volume conservation in free-surface fluid flow problems, *Computational particle mechanics*, 4, 331-343 (2016)
- 664 9. Oñate E. and Franci A. and Carbonell J.M., Lagrangian formulation for finite element analysis of quasi-incompressible fluids with reduced mass losses, *International Journal for Numerical Methods in Fluids*, 74, 699-731 (2014)
- 665 10. Franci A. and Oñate E. and Carbonell J.M., On the effect of the bulk tangent matrix in partitioned solution schemes for nearly incompressible fluids, *International Journal for Numerical Methods in Engineering*, 102, 257-277 (2015)
- 666 11. Edelsbrunner H. and Mücke E.P., Three dimensional alpha shapes, *ACM Trans Graphics*, 13, 43-72 (1999)
- 667 12. Edelsbrunner H. and Tan T.S., An upper bound for conforming delaunay triangulations, *Discrete and Computational Geometry*, 10, 197-213 (1993)
- 668 13. Oñate E. and Zárate F. and Miquel J. and Santasusana M. and Celiqúeta MA. and Arrufat F. and Gandijota R. and Valiullin K. and Ring L., A local constitutive model for the discrete element method. Application to geomaterials and concrete, *Comput Part Mech*, 2, 139-160 (2015)
- 669 14. Celiqúeta MA., Latorre S., Arrufat F. and Oñate E., Accurate modelling of the elastic behavior of a continuum with the Discrete Element Method, *Computational Mechanics*, 60, 997-1010 (2017)
- 670 15. Celiqúeta MA., Latorre S., Arrufat F. and Oñate E., An accurate nonlocal bonded discrete element method for nonlinear analysis of solids: application to concrete fracture tests, *Comp. Part. Mech*, (2019)
- 671 16. Oliver J. and Cervera M. and Oller S. and Lubliner J., Isotropic damage models and smeared crack analysis of concrete, *Second international conference on Computer Aided Analysis and Design of Concrete Structures*, (1990)
- 672 17. Casas G. and Mukherjee D. and Celiqúeta MA. and Zohdi T.I. and Oñate E., A modular partitioned discrete element framework for industrial grain distribution systems with rotating machinery, *Computational Particle Mechanics*, 4, 181-198 (2017)
- 673 18. Thornton C. and Cummins S.J. and Cleary P.W., An investigation of the comparative behaviour of alternative contact force models during inelastic collisions, *Powder Technology*, 233, 30-46 (2013)
- 674 19. Idelsohn S.R. and Oñate E. and Del Pin F., The particle finite element method: a powerful tool to solve incompressible flows with free-surfaces and breaking waves, *International Journal for Numerical Methods in Engineering*, 61, 964-989 (2004)
- 675 20. S.R. Idelsohn and J. Marti and A. Limache and E. Oñate, Unified Lagrangian Formulation For Elastic Solids And Incompressible Fluids: Applications to Fluid-Structure

- 712 Interaction Problems Via The PFEM, *Computer Methods In Applied Mechanics And En-*
713 *gineering*, 197, 1762-1776 (2008)
- 714 21. Ryzhakov P. and Oñate E. and Idelsohn S.R., Improving Mass Conservation in Simula-
715 tion of Incompressible flows, *International Journal of Numerical Methods in Engineering*,
716 90, 1435-1451 (2012)
- 717 22. Oñate E., Derivation of stabilized equations for advective-diffusive transport and fluid
718 flow problems, *Computer methods in applied mechanics and engineering*, 151, 233-267
719 (1998)
- 720 23. Pouplana I. and Oñate E. , A FIC based stabilized mixed finite element method with
721 equal order interpolation for solid-pore fluid interaction problems, *International Journal*
722 *for Numerical and Analytical Methods in Geomechanics*, 41, 110-134 (2017)
- 723 24. S.R. Idelsohn and N. Calvo and E. Oñate, Polyhedrization of an arbitrary point set,
724 *Computer Methods in Applied Mechanics and Engineering*, 92 (22-24), 2649-2668 (2003)
- 725 25. C. Chuan-Miao, Optimal points of the stresses for triangular linear element, *Numerical*
726 *Math. J. Chinese Univ.*, 2, 12-20 (1980)
- 727 26. Levine, N., Stress Sampling Points for Linear Triangles in the Finite Element Method,
728 *University of Reading, Department of Mathematics*, (1982)
- 729 27. GN. Hou and J. Wang and A. Layton , Numerical Methods for Fluid-Structure Inter-
730 action—A Review. *Communications in Computational Physics*, 12(2): p. 337-377 (2012)
- 731 28. CS. Peskin ,The immersed boundary method. *Acta Num.*, 11: p. 479-517 (2002)
- 732 29. M. Ariane and MH. Allouche and M. Bussone and F. Giacosa and F. Bernard and
733 M. Barigou and A. Alexiadis, Discrete multi-physics: A mesh-free model of blood flow in
734 flexible biological valve including solid aggregate formation, *Plose One*, 12(4):e0174795
735 (2017)
- 736 30. A.J. Gil and A. Arranz Carreño and J. Bonet and O. Hassan, The immersed structural
737 potential method for haemodynamic applications, *Journal of Computational Physics*, 229
738 (22), 8613-8641 (2010)
- 739 31. M. Cremonesi and A. Frangi and U. Perego, A Lagrangian finite element approach for
740 the analysis of fluid-structure interaction problems, *International Journal for Numerical*
741 *Methods in Engineering*, 84 (5), 610-630 (2010)
- 742 32. S. Meduri and M. Cremonesi and U. Perego and O. Bettinotti and A. Kurkchubasche and
743 V. Oancea, A partitioned fully explicit Lagrangian Finite Element Method for highly non-
744 linear Fluid-Structure-Interaction problems *International Journal for Numerical Methods*
745 *in Engineering*, 113 (1), 43-64 (2017)
- 746 33. M. Zhu and MH. Scott, Direct differentiation of the quasi-incompressible fluid formu-
747 lation of fluid-structure interaction using the PFEM, *Computational Particle Mechanics*
748 4 (3), 307-319, (2017)
- 749 34. PB. Ryzhakov and R. Rossi and SR. Idelsohn and E. Oñate, A monolithic Lagrangian
750 approach for fluid-structure interaction problems *Computational mechanics* 46 (6), 883-
751 899 (2010)
- 752 35. M.M. Joosten and W.G. Dettmer and D. Peric, Analysis of the block Gauss-Seidel solu-
753 tion procedure for a strongly coupled model problem with reference to fluid-structure in-
754 teraction *International Journal for Numerical Methods in Engineering* 78, 757-778 (2009)
- 755 36. Donea J. and Huerta A., Finite element method for flow problems. *Wiley edition, New*
756 *York* (2003)
- 757 37. E. Walhorn and A. Kölke and B. Hübner and D. Dinkler, Fluid-structure coupling
758 within a monolithic model involving free surface flows. *Computers and Structures* 25-26,
759 2100-2111 (2005)
- 760 38. R. Zorrilla and R. Rossi and R. Wüchner and E. Oñate, An embedded Finite Element
761 framework for the resolution of strongly coupled Fluid-Structure Interaction problems.
762 Application to volumetric and membrane-like structures. *Computer Methods in Applied*
763 *Mechanics and Engineering* 368, 113179 (2020)
- 764 39. M. Cremonesi and A. Franci and E. Oñate and S.R. Idelsohn, A state of the art review of
765 the Particle Finite Element Method. *Archives of Computational Methods in Engineering*
766 (2020)
- 767 40. E.M. Yettou and A. Desrochers and Y. Champoux, Experimental study on the water
768 impact of a symmetrical wedge. *Fluid Dynamics Research*, 38(1), 47-66 (2006)
- 769 41. P. Sun and F. Ming and A. Zhang, Numerical simulation of inter- actions between free
770 surface and rigid body using a robust SPH method. *Ocean Engineering* 98:32-49 (2015)

- 771 42. A. Franci, Lagrangian finite element method with nodal integration for fluid–solid in-
772 teraction. *Computational Particle Mechanics* [https://doi.org/10.1007/s40571-020-00338-](https://doi.org/10.1007/s40571-020-00338-1)
773 1 (2020)
- 774 43. Y. Li and M. Asai, Fluid-rigid body interaction simulation based on a stabilized ISPH
775 method incorporated with the impulse-based rigid body dynamics. *Transactions of the*
776 *Japan Society for Computational Engineering and Science* (2018)
- 777 44. Y. Miyagawa and M. Asai, Multi-scale bridge wash out simulation during tsunami by
778 using a particle method. *MATEC Web of Conferences* 47,02019 (2016)
- 779 45. B. Chandra and M. Asai, Verification and validation of the fluid-rigid body interaction
780 simulation by the smoothed particle hydrodynamics method. *Proceedings of computational*
781 *engineering conference JSCEs 21* (2016)
- 782 46. E. Oñate and M.A. Celigueta and S.R. Idelsohn, Modeling bed erosion in free surface
783 flows by the Particle Finite Element Method. *Acta Geotechnica* 1(4), 237–252 (2006)
- 784 47. E. Oñate and S.R. Idelsohn and M.A. Celigueta and R. Rossi, Advances in the Particle
785 Finite Element Method for the analysis of fluid–multibody interaction and bed erosion in
786 free surface flows. *Computer methods in applied mechanics and engineering* 197(19-20),
787 1777–1800 (2008)
- 788 48. Y. Dua and F. Zhou and L. Mad and J. Zheng and C. Xua and G. Chena, Consequence
789 analysis of premixed flammable gas explosion occurring in pipe using a coupled fluid-
790 structure-fracture approach. *Journal of Loss Prevention in the Process Industries* 57,
791 81–93 (2019)
- 792 49. V. Keima and P. Marxa and A. Nonna and S. Münstermann, Fluid-structure-interaction
793 modeling of dynamic fracture propagation in pipelines transporting natural gases and
794 CO₂-mixtures. *International Journal of Pressure Vessels and Piping* 175, 103934 (2019)
- 795 50. H.O. Nordhagen and S. Kragset and T. Berstad and A. Morin and C. Dørum and S.T.
796 Munkejordand, A new coupled fluid–structure modeling methodology for running ductile
797 fracture. *Computers and Structures* 94-95, 13–21 (2012)
- 798 51. T. Rabczuk and R. Gracie and J.H. Song and T. Belytschko, Immersed particle method
799 for fluid–structure interaction. *International Journal for Numerical Methods in Engineer-*
800 *ing* 81, 48–71 (2010)
- 801 52. K.G. Wang and P. Lea and C. Farhat, A computational framework for the simulation
802 of high-speed multi-material fluid–structure interaction problems with dynamic fracture.
803 *International Journal for Numerical Methods in Engineering* 104, 585–623 (2015)
- 804 53. F. Cirak and R. Deiterding and S.P. Mauchand, Large-scale fluid–structure interaction
805 simulation of viscoplastic and fracturing thin-shells subjected to shocks and detonations.
806 *Computers and Structures* 85, 1049–1065 (2007)
- 807 54. R. Talemi and S. Cooreman and H. Mahgerefteh and S. Martynov and S. Brown , A
808 fully coupled fluid-structure interaction simulation of three-dimensional dynamic ductile
809 fracture in a steel pipeline. *Theoretical and Applied Fracture Mechanics* 101, 224–235
810 (2019)
- 811 55. Y. Sudhakar and W.A. Wall, A strongly coupled partitioned approach for fluid-
812 structure-fracture interaction. *International Journal for Numerical Methods in Fluids* 87,
813 90–108 (2018)
- 814 56. T. Wick, Coupling fluid–structure interaction with phase-field fracture. *Journal of Com-*
815 *putational Physics* 327, 67–96 (2016)
- 816 57. J. Adachi and E. Siebritsb and A. Peircec and J. Desrochesd, . Computer simulation
817 of hydraulic fractures. *International Journal of Rock Mechanics and Mining Science* 44,
818 739-757 (2007)
- 819 58. S. Secchi and B.A. Schrefler, A method for 3-D hydraulic fracturing simulation. *Inter-*
820 *national Journal of Rock Mechanics and Mining Science* 178, 245-258 (2012)
- 821 59. I De-Pouplana and E. Oñate, Finite element modelling of fracture propagation in sat-
822 urated media using quasi-zero-thickness interface elements, *Computers and Geotechnics*
823 96, 103-117 (2018)
- 824 60. I De-Pouplana and E. Oñate, A FIC-based stabilized mixed finite element method with
825 equal order interpolation for solid–pore fluid interaction problems. *International journal*
826 *for numerical and analytical methods in geomechanics* 41, 110-134 (2017)
- 827 61. B. Irons and R.C. Tuck, A version of the Aitken accelerator for computer implementa-
828 tion. *International Journal for Numerical Methods in Engineering* 1, 275-277 (1969)

- 829 62. C. Antoci and M. Gallati and S. Sibilla , Numerical simulation of fluid–structure inter-
830 action by SPH. *Comput Struct* 85, 879-890 (2007)
- 831 63. B. Ren and Z. Jin and R. Gao and Y. Wang and Z. Xu , SPH-DEM Modeling of the
832 Hydraulic Stability of 2D Blocks on a Slope. *Journal of Waterway, Port, Coastal, and*
833 *Ocean Engineering* 140(6), 04014022 (2014)
- 834 64. T. Rabczuk and R. Gracie and J. Song and T. Belytschko. Immersed particle method
835 for fluid-structure interaction. *Int J Numer Meth Eng* 22, 48 (2010)
- 836 65. T. Rabczuk and T. Belytschko, A three-dimensional large deformation meshfree method
837 for arbitrary evolving cracks. *Comput Methods Appl Mech Eng* 196,2777–99 (2007)
- 838 66. K. Han and YT. Feng and DRJ. Owen. Numerical simulations of irregular particle
839 transport in turbulent flows using coupled LBM-DEM. *Comp Model Eng Sci* 18, 87 (2007)
- 840 67. T. Arikawa and K. Shimosako and N. Ishikawa. Structural failure by impulsive tsunami
841 force. *5th International Conference on Protection of Structures against Hazards* (2012)
- 842 68. A Cornejo, LG Barbu, C Escudero, X Martínez, S Oller, AH Barbat. Methodology
843 for the analysis of post-tensioned structures using a constitutive serial-parallel rule of
844 mixtures. *Composite Structures* 200, 480-497 (2018)
- 845 69. LG Barbu, A Cornejo, X Martínez, S Oller, AH Barbat. Methodology for the analysis of
846 post-tensioned structures using a constitutive serial-parallel rule of mixtures: large scale
847 non-linear analysis. *Composite Structures* 200, 480-497 (2019)
- 848 70. S Jiménez, A Cornejo, LG Barbu, S Oller, AH Barbat. Analysis of the mock-up of a
849 reactor containment building: comparison with experimental results. *Nuclear Engineering*
850 *and Design* 359, 110454 (2020)
- 851 71. C. Kassiotis, A. Ibrahimbegovic, H. Matthies. Partitioned solution to fluid-structure
852 interaction problem in application to free-surface flow. *European Journal of Mechanics,*
853 *Part B: Fluids*, 29, 510-521, (2010)
- 854 72. C. Kassiotis, A. Ibrahimbegovic, R. Niekamp, H. Matthies, Partitioned solution to non-
855 linear fluid-structure interaction problems. Part I: implicit coupling algorithms and sta-
856 bility proof, *Computational Mechanics*, 47, 305-323, (2011a)
- 857 73. U. Küttler, W. A. Wall. Fixed-point fluid–structure interaction solvers with dynamic
858 relaxation. *Computational Mechanics* 43:61–72, (2008)
- 859 74. R.K. Jaiman, N.R. Pillalamarri, M.Z. Guan. A stable second-order partitioned iterative
860 scheme for freely vibrating low-mass bluff bodies in a uniform flow. *Computer Methods in*
861 *Applied Mechanics and Engineering* 301, 187-215 (2016)
- 862 75. E.E. Knight, E. Rougier, Z. Lei, B. Euser, V. Chau, S.H. Boyce, K. Gao, K. Okubo,
863 M. Froment. HOSS: an implementation of the combined finite-discrete element method.
864 *Computational Particle Mechanics* 7, 765–787, (2020)
- 865 76. C. Yan, H. Zheng, G. Sun, X. Ge. Combined Finite-Discrete Element Method for Sim-
866 ulation of Hydraulic Fracturing. *Rock Mechanics and Rock Engineering* 49(4) (2015)